NASA CONTRACTOR
REPORT

NASA CR-16

NASA CR-1656

ADVANCED METHODS FOR CALCULATING RADIATION TRANSPORT IN ABLATION-PRODUCT CONTAMINATED BOUNDARY LAYERS

by William E. Nicolet

Prepared by
AEROTHERM CORPORATION
Mountain View, Calif. 94040
for Langley Research Center

NATIONAL AERONAUTICS AND SPACE ADMINISTRATION • WASHINGTON, D. C. • SEPTEMBER 1970

1. Report No.
✓NASA CR-1656 call no.

2. Government Accession No.

3. Recipient's Cat.

4. Title and Subtitle
✓ADVANCED METHODS FOR CALCULATING RADIATION TRANSPORT IN ABLATION-PRODUCT CONTAMINATED BOUNDARY LAYERS

5. Report Date
✓Sep~~tember 19~~70

6. Performing Organization Code

7. Author(s)
Wi~~lliam E.~~ Nicolet [illegible] ✓ACOR

8. Performing Organization Report No.
69-61 a.d.e.

9. Performing Organization Name and Address
m.e. ✓Aerotherm Corp~~oration~~
~~485 Clyde~~ Avenue
Mountain View, California 94040

10. Work Unit No.
~~124-07-18-01-23~~ omit

11. Contract or Grant No.
~~NAS1-9399~~ omit

12. Sponsoring Agency Name and Address
National Aeronautics and Space Administration
Washington, D.C. 20546

13. Type of Report and Period Covered
Contractor Report

14. Sponsoring Agency Code

15. Supplementary Notes

16. Abstract

This report describes a prediction method which can be used to obtain nongrey radiative fluxes or intensities at any point within a plane-parallel slab (for the flux calculation) or at any point on a ray (for the intensity calculation). The method was developed for the study of radiation heating phenomena in the mass injected, hypersonic boundary layer environment; however, it is not limited to such studies. The radiative properties model assumes local thermodynamic equilibrium and considers the continuum transitions, molecular bands and atomic lines of the species of the C-H-O-N elemental system. The bandless model for the molecular bands is the only approximation which is an integral part of the method. Any of the other aspects of the properties model can be made to include as much (or little) detail as desired, allowing trade-offs to be made between accuracy and computational effort.

17. Key Words (Suggested by Author(s))
High temperature gas radiation
C-H-O-N elemental system
Equilibrium
Nongrey, nonuniform slab

18. Distribution Statement
Unclassified - Unlimited

19. Security Classif. (of this report)
✓Unclassified

20. Security Classif. (of this page)
Unclassified

21. No. of Pages
90

22. Price*
$3.00

*For sale by the Clearinghouse for Federal Scientific and Technical Information
Springfield, Virginia 22151

FOREWORD

The present report describes an extended and generalized version of a radiation transport prediction method. The initial effort was done under Contract NAS9-6719 for the NASA Manned Spacecraft Center, Structures and Mechanics Division. This effort included the development of the basic radiation properties and transport models. The equilibrium chemistry capability was incorporated into the model under the present contract (NAS1-9399) for the NASA Langley Research Center, Applied Material and Physics Division.

TABLE OF CONTENTS

LIST OF FIGURES

LIST OF TABLES

LIST OF SYMBOLS

B	Planck function
b	line shape function
C	constant
c	speed of light
E	black body emissive power
e	charge on an electron
$\mathcal{E}_n$	exponential integral of order n
$F^{\pm}$	one sided radiative flux
f	oscillator strength of a line (f-number)
f	growth parameter (Eqs. (69) and (70))
f_1, f_2	arbitrary constants (Eqs. (67) and (68))
g	Gaunt factor
h	Planck's constant
j	emission per unit volume
k	Boltzmann's constant
m	mass of an electron
N_1, N_L	number of quantities, Eq. (34)
N	number density
n	principal quantum number
Q	partition function
q	net flux
Ry	Rydberg constant
S	line strength
X	ionization potential
y	spatial coordinate
$\bar{y}$	a particular spatial point

GREEK SYMBOLS

β	defined as hRy/kT
Γ	partition function ratio

LIST OF SYMBOLS (concluded)

γ	line half width
δ	path length
ε	emissivity
$\varepsilon_b^+, \varepsilon_b^-$	emissivity at wall (+) and at outer boundary (-)
μ	absorption coefficient
μ'	absorption coefficient corrected for induced emission
ν	photon frequency
ξ	Gaunt-like correction factor for non-hydrogenic atoms
τ	optical depth
φ	stretching parameter (Eq. (71))

SUBSCRIPTS

bf	bound free transition
c	quantity evaluated at the center of a line
ff	free free transition
i	species i
j	abosrbing level j
k	line k
δ	quantity evaluated at the outer edge of the layer
ν	spectral quantity

SUPERSCRIPTS

b	quantity evaluated at a spatial boundary
C	continuum quantity
D	quantity due to the Doppler effect
FF	free free transition
L	line property
PD	photodetachment transition
R	quantity due to the resonance effect
S	quantity due to the Stark effect
$\hat{\ }$	lowest level to be included in integral formulation
$\tilde{\ }$	highest level allowed under given plasma condition
$\bar{\ }$	averaged quantity

ADVANCED METHODS FOR CALCULATING RADIATION TRANSPORT IN ABLATION-PRODUCT CONTAMINATED BOUNDARY LAYERS

by William E. Nicolet
Aerotherm Corporation

SECTION 1

INTRODUCTION

The ability to predict radiant energy transport is required in order to understand the heating phenomena associated with bodies entering planetary atmospheres at high velocities. The radiation transport is important both as an energy source in direct thermal contact with the body and indirectly through the coupling between it and the thermal boundary layer. Quantitative predictions of radiative transport under these conditions require frequency dependent properties of the radiating species, a frequency dependent transport model and a method for predicting temperatures and species mole fractions, given the thermodynamic state conditions. In this study, attention is directed toward the use of an existing transport model (Ref. 1) and an existing thermodynamic equilibrium method (Ref. 2) to predict radiative transport phenomena.

Transport within the C-H-O-N elemental system is considered. This system is representative of boundary layers adjacent to most ablating bodies, and it also contains the more important radiators of many proposed planetary atmospheres. Local thermodynamic equilibrium conditions are calculated for all conditions (using thermochemical data from Ref. 3). Molecular, atomic and ionic species are considered with those which appear in the 3000^0K to the $15,000^0$K temperature range (0.1 to 10 atmospheres, pressure range) being given primary consideration.

The thermodynamic equilibrium methods are given in Section 2, the radiation properties model in Section 3 and the radiation transport model in Section 4. Predictions of radiative heating are given in Section 5 for isothermal and nonisothermal slabs. These serve to illustrate applications of the method and, in some cases, allow for comparisons with the predictions of other investigators.

SECTION 2

EQUILIBRIUM CHEMISTRY METHODS

Closed systems in equilibrium are considered. In such a system, the elemental compositions and two thermodynamic state variables are prescribed. In addition an array of candidate species and their thermochemical data are made available. From this information the equilibrium chemistry calculation is to obtain the mole fractions (or number densities) of the candidate species and the remaining state variables. Solutions to some particularly simple flow field problems, viz. downstream shockwave conditions, are also to be obtained as part of the equilibrium chemistry calculation.

2.1 THE BASIC CONCEPTS

2.1.1 Equilibrium Equations

Consider K chemical elements, N_k, introduced into a previously evacuated container. In general, these elements will interact to form a number of chemical species*, N_i (gas phase) and N_ℓ (condensed phases). If enough time has elapsed so that thermodynamic and chemical equilibrium is established, the thermodynamic state of the system, including the relative amounts of chemical species present, is completely determined if two independent thermodynamic variables are known**. This condition may be stated mathematically by examining the governing equations for such a system, and showing that the number of independent equations is equal to the number of unknown quantities.

Relations expressing the formation of the gaseous chemical species from the gaseous chemical elements may be written as follows:

$$\sum_{k=1}^{K} \nu_{ki} N_k \rightarrow N_i \tag{1}$$

Similarly, formation of condensed phase species from the gaseous elements is written:

$$\sum_{k=1}^{K} \nu_{k\ell} N_k \rightarrow N_\ell \tag{2}$$

In the above, ν_{ki} represents the number of atoms of element k in a molecule of species i (gas) or species ℓ (condensed).

---

*"Chemical species" as used here includes molecular, atomic, ionic, and electron species

** Duhem's Theorem.

If the gas phase species are assumed to individually behave as thermally perfect gases, then the equilibrium relation corresponding to reaction (1) is

$$\frac{P_i}{\prod_{k=1}^{K} P_k^{\nu_{ki}}} = K_{pi}(T)$$

or

$$\ln P_i - \sum_{k=1}^{K} \nu_{ki} \ln P_k = \ln K_{pi}(T) \tag{3}$$

where P_k denotes partial pressures and $K_{pi}(T)$ is the equilibrium constant for the formation reaction (1) of species N_i. For each candidate condensed phase species

$$-\sum_{k=1}^{K} \nu_{k\ell} \ln P_k \overset{<}{=} \ln K_{p\ell}(T) \tag{4}$$

where

$=$ indicates the existance of the condensed phase species N_ℓ in equilibrium with gas phase species, and

$<$ indicates that the condensed phase species N_ℓ will not be present in equilibrium

For each chemical element introduced into the system, the conservation of atoms dictates that the amount of any element k in the gas and condensed phases (regardless of molecular configuration) must sum to the total amount of element k in the system. Mathematically, this may be written, for each element k, as

$$\begin{array}{l}\text{Mass fraction}\\ \text{of element k}\\ \text{input to the}\\ \text{system}\end{array} = \frac{\mathcal{M}_k}{\mathcal{M}P} \sum_{i=1}^{I} \nu_{ki} P_i + \frac{\mathcal{M}_k}{\mathcal{M}} \sum_{\ell=1}^{L} \nu_{k\ell} X_\ell \tag{5}$$

where $\mathcal{M}$ is a composite system molecular weight* defined by

$$\mathcal{M} = \sum_{i=1}^{I} \frac{P_i}{P} \mathcal{M}_i + \sum_{\ell=1}^{L} X_\ell \mathcal{M}_\ell \qquad \text{units of } \frac{\text{grams of system}}{\text{moles of gas}}$$

and where X_ℓ is a mole fraction of condensed phase species ℓ defined as

$$X_\ell = \frac{\text{molecules of condensed species } \ell}{\text{total gas phase molecules } i}$$

In addition, for the gas phase species, there exists the requirement that the partial pressures must sum to the total system pressure.

$$\sum_{i=1}^{I} P_i = P \tag{6}$$

Mixture thermodynamic properties, such as specific enthalpy, are related to the species concentrations by equations of the form

$$h = \frac{1}{\mathcal{M}P} \sum_{i=1}^{I} P_i h_i + \frac{1}{\mathcal{M}} \sum_{\ell=1}^{L} X_\ell H_\ell \tag{7}$$

Consider now the number of independent equations for the system. The number of gas phase equilibrium relations (3) is equal to the number of gas phase species I minus the number of elements K (because equations (3) are trivial i=k). In addition, there exists a relation such as (4) for each of the L candidate condensed phase species in the system. Note that the system temperature is contained implicitly in Equations (3) and (4) through the temperature dependence of the equilibrium constants. There are K conservation of elements equations (5), one for each atomic element introduced into the system. The requirement that the partial pressures sum to the system pressure (6) contributes one additional equation. For any additional thermodynamic properties of the mixture (enthalpy, entropy, etc.), there exists equations such as (7).

---

*This is the molecular weight appropriate to the ideal gas equation of state if condensed phases are present.

Consider next the variables appropriate to this formulation of the problem. The relative concentrations of the I species in the gas phase are given by the P_i's and the amounts of the L candidate condensed phase species are given by X_ℓ (all of which may be zero). In this formulation, the composite system molecular weight, $\mathfrak{M}$ is also a variable. There are one each of the mixture thermodynamic variables T,p,h,s, etc. The number of variables and available independent equations may be summarized as

TABLE I - CLOSURE OF CHEMICAL SYSTEM

VARIABLES	NO. OF SUCH VARIABLES	EQUATION NUMBER	NO. OF SUCH EQUATIONS
P_i	I	(3)	I - K
X_ℓ	L	(4)	L
$\mathfrak{M}$	1	(5)	K
P	1	(6)	1
T	1		
h, s, p	n	of the type (7)	n
total variables	I+L+n+3	total equations	I+L+n+1

Thus, there are two less equations than there are variables, and so if two independent variables are specified (e.g., P and T) in addition to the elemental composition, then closure is obtained and the chemical and thermodynamic state of the system may, in principal, be determined.

2.1.2 Base Species

Equations 1 to 5 describe the equilibrium reaction equations in terms of the formation of species from atomic elements. Thus, the reactants are elements and the products are usually molecules. This scheme has the advantage of formal simplicity; however, it is unnecessarily restrictive and can lead to certain classes of computational difficulties.

Equations 1 to 5 can equally well describe equilibrium conditions in terms of the formation of species from another set of species (the base species -- from Reference 4). In this reinterpretation of the equilibrium equations, each atomic element is replaced by an arbitrarily selected (base) specie. Valid equilibrium solutions are still obtained provided that (1) all other species can be formed from the set of base species and (2) no balanced reactions can be written involving only base species.

2.1.3 Ionized Systems

Ionization is included in the equilibrium equation by allowing ionic and an electron species in the set of candidate species and an electron "element" in the set of base species. Each specie (free) electron consists of one elemental electron. The ions are formed from one (or more) neutral base species and one or more lost (negative ν_{ij}) electron elements. In this scheme the elemental mass balance (Eq. 5) for the electron is also a charge balance. Thus, the specification of a non zero value of the elemental electron concentration yields a nonneutral system; where as, a zero value yields a neutral system.

2.1.4 Equilibrium Constants

At equilibrium, the second law requires that the independent reactions occur without change in free energy. Therefore

$$G_j = \sum_i \nu_{ji} G_i \tag{8}$$

where the G_j are the partial molar free energies of the species (also referred to as the chemical potentials). The change in free energy is, by definition, equal to the isothermal reversible work performed by a steady flowing system in passing from one state to another. On this basis it is possible to relate the G_j to the standard-state free energies, G_j^o, that is, the free energy of the species at the same temperature but undiluted and at one atmosphere pressure. Thus

$$G_j - G_j^o = \left[-\int_{P^o}^{P} vdP \right]_{\text{isothermal, reversible}} \tag{9}$$

where p^o is one atmosphere. For a gas obeying the perfect gas law

$$G_j - G_j^o = - RT \ln p_j \tag{10}$$

if p_j is in units of atmospheres. Likewise, for an incompressible condensed phase containing only one species

$$G_\ell - G_\ell^o = \frac{1 - p}{\rho_\ell} \tag{11}$$

When more than one condensed species coexists in a phase, the work of mixing must be included. For an ideal mixture*

$$G_\ell - G_\ell^o = \frac{1 - P}{\rho_\ell} - RT \ln X_\ell \tag{12}$$

where X_ℓ is the mole fraction of species ℓ in the mixture.

In environments of general concern in high-temperature thermodynamics Eqs. (10) and (11) are generally employed and, in addition, $(1-P)/\rho_\ell$ is assumed negligible in relation to the gas-phase work terms. On this basis, simplified equilibrium constant relations are obtained from Eqs. (8) and (10) for gas and condensed species (sub j or ℓ).

$$\ln K_{p_j} = - \frac{\Delta G_j^o}{RT} \tag{13}$$

where the standard-state free energy change of the formation reaction for species j (or ℓ) is defined by

$$\Delta G_j^o = G_j^o - \sum_i \nu_{ji} G_i^o \tag{14}$$

and the partial pressure of condensed species will be taken as one atmosphere in order that Eq. (10) will indicate no work of compression.

The standard state free energy is a function of temperature only and is obtained for each molecular species from

$$G_j^o = H_j^o - TS_j^o \tag{15}$$

where enthalpies are obtained relative to some chemical base state, often the elements in their most natural form at 298°K and one atmosphere (JANAF base state). If any other base state is consistently adopted, the ΔG_j^o will be unaffected.

The enthalpy and entropy of the species are conveniently expressed in terms of the specific heats, viz.

$$H_j^o = H_{j_o}^o + \int_{T_o}^{T} C_{p_j}^o \, dT \tag{16}$$

---

*The ideal mixture assumption is satisfied by a mixture above which vapor pressures are proportional to mixture mole fractions and whose vapors obey the perfect gas law.

and

$$S_j^o = S_{j_o}^o + \int_{T_o}^{T} \frac{C_{p_j}^o}{T}\, dT \tag{17}$$

where the o subscript refers to the chemical base-state. Thus, Eqs. (13) to (17) can be used to obtain the equilibrium constants, provided only that the specific heats of the reacting species are known, along with base values of entropy and enthalpy. The specific heats for each specie can either be obtained directly from tabulations which are available (e.g. Refs. 5, 6, and 7) or can be calculated from the relation

$$C_{p_j}^o = 2RT \left(\frac{\partial \ln Q_i}{\partial T}\right)_p + RT^2 \left(\frac{\partial^2 \ln Q_j}{\partial T^2}\right)_p \tag{18}$$

where Q_j is the partition function of the species and can be evaluated from statistical principals and spectroscopic data.

2.1.5 Partition Functions

The Partition Function of a species can quite generally be written as

$$Q_j = \sum_{\substack{\text{Energy}\\ \text{Levels}}} g_i \exp\left(-\frac{\varepsilon_i}{kT}\right) \tag{19}$$

where the summation extends over all energies accessible to the species and whose g_i and ε_i are the degeneracy and energy of the $i^{\underline{th}}$ level, respectively. The energy of any gaseous species (atomic or molecular) can be written as the sum of two independent components, one of which is related to transitional motion, the other to internal motions.

$$\varepsilon_i = \varepsilon_{\text{translation}} + \varepsilon_{\text{internal}}$$

Therefore, the partition function can be factored into components representing translational and internal contributions, viz.

$$Q_j = Q_{j\,\text{translation}} \cdot Q_{j\,\text{internal}}$$

For the translational motion, the energy levels are sufficiently close together to allow the summation in Eq. (19) to be replaced by an integration. This yields the closed form expression

$$Q_{j_{\text{translation}}} = \left(\frac{2\pi M_j RT}{Na^2 h^2} \right)^{3/2} \frac{RT}{P} \qquad (20)$$

for the translational contribution to the partition function. Here, Na is Avogadro's number and the rest of the symbols have their usual meanings.

For a monatomic species (atomic or ionic), the internal contribution to the partition function is obtained by summing over the electronic energy levels which can be occupied by the particle. For all systems except that of an isolated particle in an enclosure of infinite volume, the levels which can be occupied correspond to electronic shells relatively close to the nucleus*. The effect on the partition function summation can be expressed as either

$$Q_{j_{\text{internal}}} = \sum^{\varepsilon_{\text{max}}(P,T)} g_i \exp\left(- \frac{\varepsilon_i}{kT}\right) \qquad (21a)$$

or

$$Q_{j_{\text{internal}}} = \sum_{\substack{\text{core} \\ \text{levels}}} g_i \exp\left(- \frac{\varepsilon_i}{kT}\right) + \phi(T,P) \cdot \sum_{\substack{\text{excited} \\ \text{levels}}} g_i \exp\left(- \frac{\varepsilon_i}{kT}\right) \qquad (21b)$$

where $0 \leq \phi(T,P) \leq 1$

and where the summation in Eq. 21a includes only levels up to some maximum level specified as a function of the temperature and pressure. An alternate expression given in Eq. 21b includes the summation over a prescribed number of core levels (which the particle can always occupy) plus a specified fraction, $\phi(T,P)$, of the contribution due to the excited levels. The selection

---

* Electrons in the uppermost shells are excluded by the interaction between them and other particles in the system.

of the cutoff can significantly effect the values of the partition functions at high temperatures ($T \geq O(17,000\ ^{\circ}K)$ for N). However, the effect on the mole fractions of the dominant species in the mixture is generally not dramatic (order of a few percent). Indeed, satisfactory results for air were obtained by Gilmore (Ref. 8) by setting $\phi(T,P) \equiv 0$ in Eq.(20b), thereby eliminating the pressure dependence entirely. A rational for this fortuitous behavior has been given by Hunt and Sibulkin (Ref. 9).

For diatomic species the internal energy levels can be further divided into a sum of independent electronic and vibrational-rotational components. This allows $Q_{j_{internal}}$ to be factored into

$$Q_{j_{internal}} = Q_{j_{vib\text{-}rot}} \cdot Q_{electronic} \tag{22}$$

where the electronic contribution to the partition function is evaluated directly from Eq. (19) as was done for the monatomic species. The vibrational-rotational contribution to the partition can be expressed as

$$Q_{j_{vib\text{-}rot}} = \sum_{v} \exp\left(\frac{-G(v)hc}{kT}\right) Q_{rot}^{(v)} \tag{23}$$

where

$$Q_{rot}^{(v)} \approx \frac{kT}{hcB(v)} \tag{24}$$

and where $G(v)$ is the vibrational term of the $v^{\underline{th}}$ vibrational level relative to the lowest vibrational level, and $B(v)$ is the corresponding rotational constant.

2.2 SOLUTION PROCEDURE

2.2.1 Basic Technique

Equations (3), (5) and (6) make up the basic system to be solved, when temperatures and pressures are specified. If temperature is to be replaced by some other thermodynamic state variable, a defining relation of the form of Eq. (7) must also be included in the system. If an additional set of relations (e.g., the Rankine-Hugoniot equations -- see Section 2.2.3) are to be satisfied simultaneously, these must also be included in the system. The equations are highly nonlinear and, consequently, an iterative solution procedure is required.

The number of unknowns could immediately be reduced by I-K through the direct substitution of (5), as solved for P_i, into the other relations. It proves advantageous, however, to continue to treat the full set of equations, and to subsequently utilize this substitution during the iterative convergence procedure. The solution of these simultaneous nonlinear algebraic equations is based on Newton-Raphson iteration. Since this procedure is accelerated by casting the equations into a more linear form (via transformations, substitutions, etc.) it is well to examine the set of equations above. Equations (5) and (6) are linear relations between P_i and $\mathcal{M}$. In contrast, equations of the form (3) are linear in $\ell n\ P_i$, $\ell n\ P_k$ and $\ell n\ K_{pi}$, the latter variable veing approximately linear in 1/T.

The solution procedure takes advantage of this situation by treating those species which are significant in the mass and pressure balances (5) and (6) in terms of P_i and the less significant species in terms of their $\ell n\ P_i$.

The Newton-Raphson procedure, as presently utilized, can be summarized by considering a set of equations of the general form

$$f_j(x_1, x_2, \ldots, x_i, \ldots) = 0$$

At any point in the solution procedures there exists a set of estimates, x_i^*, for all the variables which will in general not satisfy all of the relations and will lead to a non-zero value of the f_j, namely, ε_j. The Newton-Raphson method proceeds to "drive" these errors toward zero by evaluating the change in each unknown variable, Δx_i, which would reduce all the errors to zero if the functions, f_j, were linear. The linear approximation is based on the current values of the unknown variables and the corresponding array of values of the partial derivatives $\partial f_j/\partial x_i$. Thus

$$df_j = \sum \frac{\partial f_j}{\partial x_i} dx_i \tag{25}$$

which is locally correct and is integrated to

$$(\Delta f_j)^* \simeq \sum \left(\frac{\partial f_j}{\partial x_i}\right)^* (\Delta x_i)^*$$

in the linear approximation. The solution of (25) is

$$dx_i = \sum \frac{\partial x_i}{\partial f_j} df_j \tag{26}$$

where the array of partial derivatives appearing in (26) is simply the matrix inverse of the array in (25). The formulation of the partial derivatives uses the variables, $\ell n\ P_i$,* $\ell n\ T$ and $\ell n\ \mathfrak{n}$ and (26) yields, for example,

$$d(\ell n\ P_i) = \sum \frac{\partial\ \ell n\ P_i}{\partial f_j}\ df_j$$

which if taken as linear all the way to solution yields

$$n\ \frac{P_i^{**}}{P_i^{*}} = (\Delta\ \ell n\ P_i)^* \simeq \sum \left(\frac{\partial\ \ell n\ P_i}{\partial f_j} \right)^* (-\varepsilon_j)^* \qquad (27)$$

since the desired change in the functions is simply the negative of the error. An alternate, but equally valid relation is

$$dP_i = P_i \sum \frac{\partial\ \ell n\ P_i}{\partial f_j}\ df_j$$

which if taken as linear all the way to solution yields

$$P_i^{**} - P_i^{*} = \Delta P_i^{*} \approx P_i^{*} \sum \left(\frac{\partial\ \ell n\ P_i}{\partial f_j} \right)^* (-\varepsilon_j^{*}) \qquad (28)$$

Equation (28) is used for all species significant in mass balances and (27) for the others.

2.2.2 Restriction on Corrections

The set of correction $(\Delta x_i)^*$ can be thought of as a vector in the space of the independent variables which is added to the current vector approximation x_i^* to yield a new estimate x_i^{**}. Experience has shown that it is frequently unwise to proceed along this correction vector the full amount indicated by (27) or (28). Rather, it is better to proceed a limited way,

---

*The choice of $\ell n\ P_i$ permits a matrix reduction by the use of the simple algebraic substitution, as previously mentioned, prior to matrix inversion.

although preserving the same direction. At other times, it is expedient to depart from this vector, and seek another based on freezing the value of some variable and eliminating a corresponding equation.

The scaling of the correction vector is such as to limit changes in the partial pressures of major species to increases of one order of magnitude and decreases of three orders of magnitude, and changes of temperature to approximately 20 percent.

Molecular weight, temperature and condensed phase concentration corrections are frozen and a new correction vector generated if the initial set of corrections indicate excessive temperature or molecular weight excursions, a contradictory temperature change, or negative corrections on newly introduced condensed species.

The formulation of these and other scaling and freezing criteria is an essential feature of the calculational procedure. Because of these features, convergence is virtually assured for well formulated, physically unique problems.

2.2.3 Incorporation of Simple Flow Field Systems

The flow variables downstream of a standing shock wave are usually required for problems involving hypersonic flow fields. The governing Rankine-Hugoniot equations are readily incorporated in the set of equations governing the equilibrium chemistry to yield a useful calculational procedure.

Consider flow through an oblique shock wave with upstream conditions known and downstream conditions unknown.

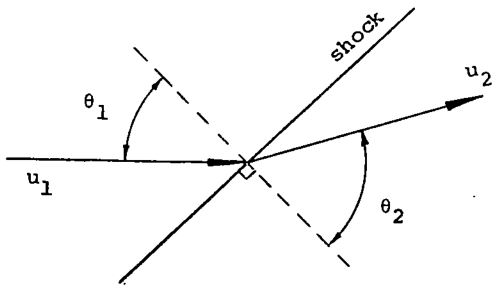

Figure 1. Shock Wave Configuration

Equations expressing the conservation of mass, energy, and momentum (independent of events "in" the shock) may be written as follows:

Mass

$$\rho_2 u_2 \cos\theta_2 = \rho_1 u_1 \cos\theta_1 \tag{29}$$

Energy

$$h_2 + \frac{1}{2} u_2^2 = h_1 + \frac{1}{2} u_1^2 \tag{30}$$

Normal Momentum

$$P_2 + \rho_2 u_2^2 \cos^2\theta_2 = P_1 + \rho_1 u_1^2 \cos^2\theta_1 \tag{31}$$

Tangential Momentum

$$\rho_2 u_2^2 \cos\theta_2 \sin\theta_2 = \rho_1 u_1^2 \cos\theta_1 \sin\theta_1 \tag{32}$$

The four conservation equations, as written above, involve five unknowns: θ_2, u_2, P_2, ρ_2, h_2. However, the thermodynamic variables on the downstream side of the shock are related by the chemical equilibrium and thermodynamic state relations discussed in Section 2.1.1. Recall that these relations were sufficient to completely define the thermodynamic and chemical state of a system given the elemental composition and any two independent thermodynamic state variables (e.g., ρ_2 as a function of P_2 and h_2).

Thus, the chemical equilibrium and thermodynamic state relations, plus the four conservation Equations (29) through (32) are sufficient to determine the condition downstream of a shock wave if all upstream conditions are known. Solution to this set of equations are readily obtained by the method described in Sections 2.2.1 and 2.2.2.

The shock wave equations can be generalized to describe the hypersonic flow about a sphere. The shock layer in the stagnation region can be characterized by

$$\left.\begin{array}{l} P(y) = \text{const.}, \quad T(y) = \text{const.}, \quad \text{(inviscid region)} \\ \text{where} \\ \qquad\qquad \delta \le y \le 0 \\ \text{and} \\ \dfrac{\delta}{R} \simeq \dfrac{\rho_1}{\rho_2 (1 + \sqrt{8\rho_1/3\rho_2})}, \quad (R = \text{radius of shock}) \end{array}\right\} \tag{33}$$

provided that radiation losses from the shock layer are small compared to the flow energy, i.e., $Q_{rad} << \rho_1 u^3/2$. When valid, Equations (29) to (33) provide all the necessary inputs for a useful class of radiation heating problems. Even when the radiation losses are large, solutions to this set of equations are often useful as reference conditions.

2.3 THE CHEMICAL EQUILIBRIUM PROGRAM (EQUIL)

The solution procedure of Section 2.2 has been automated to solve Equations (3) to (7) employing the base species concept and including a conservation of charge relation when required (for ionized systems). The equilibrium constants are obtained using the method of Section 2.1.4. The specific heats for each specie are input through two curve-fits - one for each of two allowable temperature ranges - of the form

$$C^{o}_{p_i} = F_3 + F_4 T + F_5/T^2$$

where the coefficients are generally established by least-squares fits to tabulations of $C^{o}_{p_i}$ versus T data such as that given in the JANAF tables (Ref. 5.). Tables of the coefficients are given in Reference 3 for many species of interest. The additional data required, heats of formation and the base state conditions, are also generally available in tabulations such as Reference 5.

The program has been run extensively as a part of the Aerotherm Chemical Equilibrium (ACE) program (which is of equal accuracy but greater generality). Computational times on computers such as the UNIVAC 1108 or CDC 6600 are on the order of two to three seconds per solution.

SECTION 3

ABSORPTION COEFFICIENTS OF THE BOUNDARY LAYER SPECIES

3.1 IMPORTANT ABSORPTION MECHANISMS

The spectral absorption coefficient for a plasma consisting of a mixture of elements is in general

$$\mu_\nu = \sum_{i=1}^{N_1} \mu_i^C(\nu) + \sum_{k=1}^{N_L} \mu_k^L(\nu) \tag{34}$$

where the first term represents the continuum contribution with its summation taken over all continuum transitions (N_1), and the second term represents line contributions with the summation taken over all the lines (N_L). For the plasma conditions of interest, the important continuum transitions include atomic photoionization, photodetachment, free-free transitions, photodissociation and molecular photoionization in approximately a decreasing order of importance. The atomic line transitions are very important. The molecular band systems can be important for some conditions.

3.1.1 Atomic Continuum Transitions

In general, continuum contributions depend on the plasma state (to a satisfactory approximation) only through the populations of the absorbing levels, viz.

$$\mu_i^C(\nu) = \sum_j N_{ij}\sigma_{ij}^C(\nu) \tag{35}$$

where N_{ij} is the number density of the absorbing level and $\sigma_{ij}^C(\nu)$ is its cross-section. The number densities must be obtained from thermodynamic state calculations and the cross sections either from quantum mechanical calculation or experiment.

Hydrogen cross sections are well understood, exact values being available (Ref. 10)

$$\sigma_{bf} = \frac{2^6\pi^4}{3\sqrt{3}}\,\frac{me^{10}}{ch^6 n_a^5 \nu^3}\,g_{bf} \tag{36}$$

$$\sigma_{ff} = \frac{2^4 \pi^2 e^6}{3\sqrt{3}\, hc(2\pi m)^{3/2}} \frac{N_e}{(kT)^{1/2} \nu^3} g_{ff} \tag{37}$$

where the subscripts bf and ff refer to bound-free (photoionization) and free-free transition, respectively. The quantity n_a is the principal quantum number of the absorbing level; N_e is the number density of free electrons; g_{bf} and g_{ff} are Gaunt factors which are available in tabular form (Ref. 10), and the other symbols have their usual meanings. The Gaunt factors are often taken to be unity (a good approximation) or expressed in terms of shell averages ($\bar{g}_{ff}$). This allows a closed form expression to be obtained for the free-free contribution for the z,z+1 stage of ionization (Ref. 11), viz.

$$\mu_i^{FF}(\nu) = \frac{32}{3\sqrt{3}} \left(\frac{\pi^2 e^6}{2hc}\right) \frac{kT(z+1)^2}{(h\nu)^3} \frac{Q^{z+1}}{Q^z} \exp\left(-\frac{x^z}{kT}\right) \bar{g}_{ff} \tag{38}$$

where Q^z and Q^{z+1} are the electronic partition functions of the atom and its ion, respectively, where x^z is the ionization energy of the atom, where z+1 is the charge on the residual ion. The photoionization contribution is also simplified, viz.

$$\mu_i^{PI}(\nu) = \mu_i^{FF}(\nu) \sum_{\nu_{n_a} < \nu} \frac{1}{n_a^3} \exp\left(\frac{h\nu_{n_a}}{kT}\right) \tag{39}$$

where ν_{n_a} is the threshold frequency of the level n_a. At sufficiently high values of n_a, the levels are so closely spaces that the summation can be approximated by an integration (see Ref. 12, for example)

$$\mu_i^{PI}(\nu) \approx \mu_i^{FF} \left\{ \exp(hRy/n^2 kT) - \exp(hRy/\tilde{n}^2 kT) \right\} \tag{40}$$

where n is the lowest level to be included in the integral formulation and $\tilde{n}$ is the highest level allowed at the given plasma condition.

In the case of the heavy atoms, no exact cross sections are available. The most widely accepted method of calculating them is the "quantum defect" approximation as put forth by Burgess and Seaton (Ref. 13). This method has been used by Armstrong, Johnston and Kelly (Ref. 14, see also Refs. 15, 16, and 17) to obtain the level cross sections for the levels of N and O. A compilation of this work is available (Ref. 11) in which "effective cross sections" ($\equiv \mu_i(\nu)/N_i$) are tabulated.

A useful approximation for the heavy atom contributions at low frequencies has been proposed by Biberman and Norman (Ref. 15). They also use the quantum defect method but have obtained an approximate, closed form solution for the total contribution. Their results are presented in terms of two correction factors to be applied to the hydrogenic formula, viz.

$$\mu_i^{PI,FF}(\nu) = \Gamma\xi(h\nu,T)\left[\mu_i^{PI,FF}(\nu)\right]_{hydrogenic} \tag{41}$$

where $\Gamma = 2Q^{z+1}/Q^z$. Tabulated values of $\xi(h\nu,T)$ are available (Ref. 15) for many different atoms. The absorption coefficients calculated from Equation (41) show surprisingly good agreement with the fully detailed ones of Armstrong et.al.(Ref. 14). Tabulated values of the effective cross sections of C and C+ as obtained from Equation (41) are available (Ref. 11).

Figure 2 shows nitrogen continuum cross sections taken from References 14 and 15 and illustrates the dominant importance of the photoionization edges.

3.1.2 Atomic Line Transitions

The absorption coefficients of the atomic line transitions depend on the plasma condition both through the population of the absorbing level and also through the shapes of the lines. Thus,

$$\mu_{k(j)}^{L}(\nu) = \frac{\pi e^2}{mc} f_{k(j)} N_{ij} b_{k(j)}(\nu,T,P,x_1,x_2\ldots) \tag{42}$$

where $f_{k(j)}$ is the oscillator strength of the k^{th} line in the j^{th} series of lines and $b_{k(j)}(\nu,T,P,x_1,x_2,\ldots)$ is the line shape and is a function of frequency and the plasma condition. The line shape obeys the normalization condition (omitting the explicitly written functional dependence on the plasma condition for brevity)

$$\int_0^\infty b_k(\nu)\,d\nu = 1$$

but otherwise is free to take on a variety of functional forms depending upon the species involved and the broadening mechanisms (or combination of mechanisms).

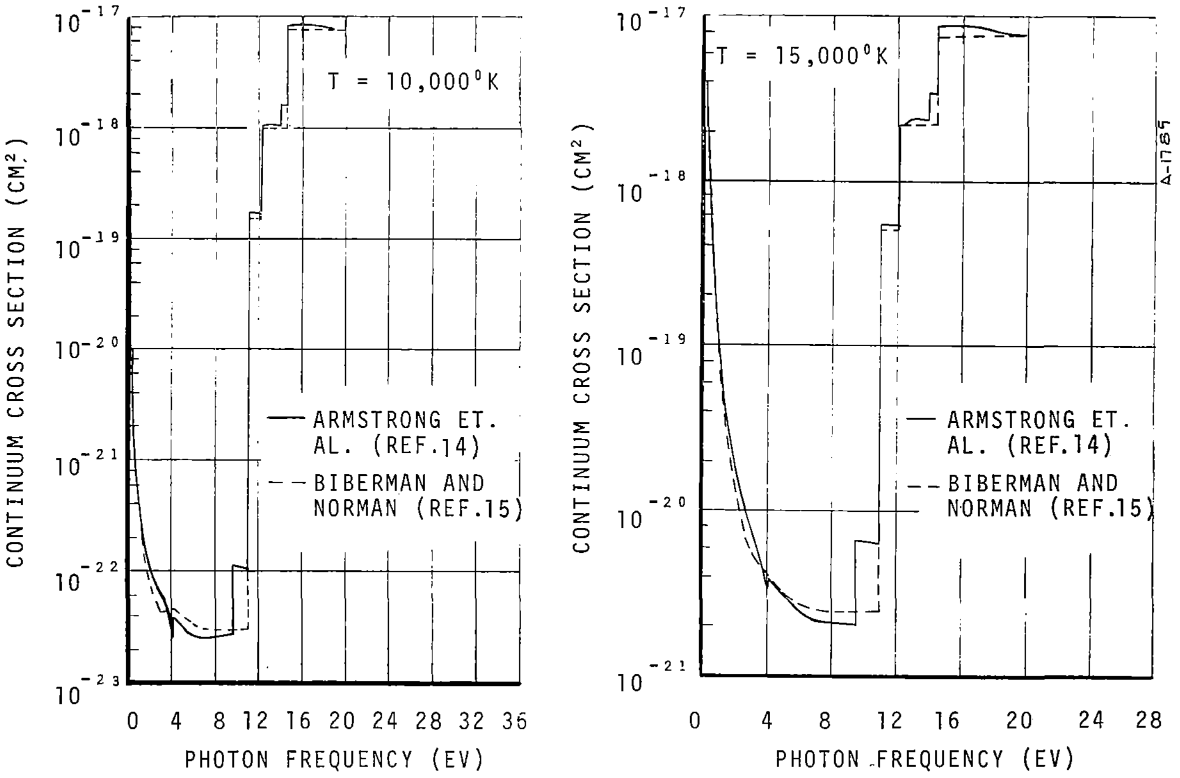

Figure 2. Continuum Cross Sections of Nitrogen

For the heavy atomic species, the dominant broadening mechanism is Stark broadening by electron impacts. Following Armstrong et.al.(Ref. 14) it is assumed that each multiplet can be treated as a line with a Lorentz shape,viz.

$$b_k(\nu) = \frac{\gamma_k^S/\pi}{(\nu-\nu_k)^2 + (\gamma_k^S)^2} \tag{43}$$

where ν_k is the frequency of the line center and γ_k^S is the Stark (half) half-width which is a function of the plasma condition. Corrections to Equation (43) due to J-splitting and effects due to ion perturbers are often ignored.

The (half) half-widths, γ_k^S, can be calculated from the electron impact approximation. Griem (Ref. 18) has worked out the proper formulation and tabulates data for many transitions and for several elements. Wilson and Nicolet (Ref. 11) have performed the calculations* for all the important transitions in N, N+, O, O+, C and C+. A comparison given by Wilson and Greif (Ref. 19) shows that the data of Reference 11 compares favorably with that of Reference 18. Page et.al.(Ref. 20) report that the (half) half-widths from Reference 11 can be approximated as

$$\gamma_K^S(T) \approx \left(\frac{T}{T_o}\right)^n \gamma_K^S\left(T_o\right) \tag{44}$$

where n = 0.25, 0.46 and 0.43 for nitrogen, oxygen and carbon, respectively.

For many plasma conditions of present interest, the degree of ionization is very low. Under such conditions, resonance broadening can be greater than Stark broadening, yielding lines with Lorentz shapes having (half) half-widths which can be calculated in an impact approximation (Ref. 9) as

$$\gamma_k^R \cong 3\pi\left(\frac{g_\ell}{g_u}\right)\left(\frac{e^2 f_{res}}{2\pi m\nu_{res}}\right)N_a \tag{45}$$

Here f_{res}, ν_{res}, g_ℓ and g_u all belong to the resonance line and are, respectively, the absorption oscillator strength, the center frequency, the lower statistical weight and the upper state statistical weight. N_a is the number of perturbing atoms per unit volume.

---

*It should be noted that until recently an erroneous approximation was usually made in this calculation (see Ref. 11 for a discussion of this point) which resulted in half-widths which were much too large.

The broadening mechanisms for atomic hydrogen require exceptional treatment. The Stark splitting of hydrogen lines is much greater than that of other spectra (Ref. 21). This effect is connected with the accidental degeneracy in hydrogen whereby terms of the same principal quantum number but different orbital quantum numbers have (very nearly) the same energy. Further, it is known that broadening caused by ion perturbers is not negligible compared to that caused by electron impacts (see Ref. 22). Thus, the Lorentz line shapes often cannot be used. The line shape in the core region of each of the important hydrogen lines was obtained by Griem, Kolb and Shen (Ref. 22) and is available in numerical form.* Asymptotic equations are given by Griem (Ref. 18) for the shape of the far wings, viz.

$$b_k(\nu) = \text{const.}\ \frac{S_k(\alpha(\nu))}{\nu^2\sqrt{2.61eN_e{}^{2/3}}} \tag{46}$$

and

$$\lim_{\alpha \to \infty} S_k(\alpha) = \frac{C_k}{\alpha^{5/2}}\left[1 + R_k(N_e,T)\sqrt{2.61eN_e{}^{2/3}\alpha}\right] \tag{47}$$

The parameter $\alpha(\nu)$ is defined as

$$\alpha(\nu) = \frac{\Delta\lambda(\text{Å})}{2.61 \times 10^{-8}eN_e{}^{2/3}} \approx \frac{\text{const.} \times (\nu - \nu_k)}{2.61 \times 10^{-8}\nu_k{}^2eN_e{}^{2/3}} \tag{48}$$

and values of C_k and R_k are available in Ref. 18. For transitions involving highly excited levels, Griem (Ref. 23) has shown that electron impact broadening is dominant. Thus, the Lorentz shape can be used with the (half) half-widths taken from Griem (Ref. 23), viz.

$$\gamma_k^S = \text{const.}N_e\log_{10}\left(\frac{3 \times 10^6 T}{n_u^2 N_e}\right)\frac{n_\ell^5 + n_u^5}{T^{1/2}} \tag{49}$$

where n_ℓ and n_u are the principal quantum numbers of the lower and upper levels of the transition, respectively.

---

*The Griem et.al. (Ref. 22) line shapes have recently been revised by Kepple (Ref. 24). Comparisons cited in Ref. 24 indicate excellent (~10%) agreement between calculated and measured half widths.

The lines of all the species can also be broadened by the Doppler effect. Hunt and Sibulkin (Ref. 9) have recently pointed out that it is important to include this mechanism for some plasma conditions of interest. The Doppler broadened line acquires the shape

$$b_k(\nu) = \frac{1}{\sqrt{\pi}} \frac{\sqrt{\ln 2}}{\gamma_k^D} \exp\left[-\frac{(\nu - \nu_k)^2 \ln 2}{(\gamma_k^D)^2}\right] \tag{50}$$

where γ_k^D is the Doppler (half) half-width and is given by

$$\gamma_k^D = \frac{\nu_k}{c} \sqrt{\frac{2kT}{m_i} \ln 2} \tag{51}$$

where m_i is the mass of the radiating particle. In order for this mechanism to participate in a meaningful way in transport calculations, γ_k^D must be very much larger than $\gamma_k^S + \gamma_k^R$. This effect occurs because the Doppler wings decay exponentially; whereas, the Lorentz wings decay quadrically, and most of the radiant energy is (usually) transported in the wings.

Some of the atomic lines can be treated like a continuum rather than individually. The high lines* in a given series always become overlapped as they approach their series limit. Armstrong (Ref. 25) has shown that the photoionization threshold can be shifted to lower frequencies to account for the contributions from these lines, viz.

$$\Delta h\nu \sim \left(N_e^2/kT\right)^{1/7}$$

where $\Delta h\nu$ is the shift in terms of photon energy.

Lines belonging to high series** can also be treated as a continuum contribution. They become overlapped at low frequencies; in addition, they are usually weak. Integral formulations for the contributions of these lines have been obtained in a variety of investigations (Refs. 9 and 26, for example).

---

*The high lines in a series are associated with transitions which have upper levels with large principal quantum number.

**The high series are associated with transitions which have lower levels with large principal quantum numbers.

All approximate the line strengths by shell averaged hydrogenic values. This is consistent with the fully detailed calculations (Ref. 14). For a uniform and optically thin plasma, Vorobyov and Norman (Ref. 26) have obtained the total emission per unit volume (j) of all the transitions originating at or above the level k, viz.

$$j = \text{const.}\ \frac{1}{4\beta} \exp\left(-\frac{X^z}{kT}\right)\Gamma\left[\frac{1}{\beta}\left(\exp\frac{\beta}{n_a^2} - \exp\frac{\beta}{\tilde{n}^2}\right) - \left(n_a^{-2} - n^{-2}\right)\exp\frac{\beta}{\tilde{n}^2}\,N_i\right] \tag{52}$$

where $\beta = hRy/kT$, where z is the charge of the atom, X^z its ionization potential and $\tilde{n}$ the highest level allowed at the given plasma condition. Vorobyov and Norman (Ref. 26) do not discuss the spectral distribution of the intensities thus obtained; however, Hunt and Sibulkin (Ref. 9) have obtained a somewhat similar equation and indicate that the distribution should be the same as that for free-free transitions. If one interprets high series as transitions of nearly free electrons, then the plausibility of such an argument is seen.

Even for strong and/or isolated lines, a fully detailed evaluation of Equations (34), (42), and (43) is often not required; rather, the line group approximation can be utilized. Initially, the frequency range of interest is divided into a number of increments. Each increment defines as a line group those lines which are centered within it. The line contributions at a frequency point within a frequency increment is obtained by summing over only those lines within its line group. This approximation usually yields a significant simplification. Its region of validity will be discussed in Section 3.2.2.

3.1.3 Molecular Band Transitions

The rotational lines situated in molecular band systems can also be treated as a pseudo continuum, rather than individually, for many plasma conditions of interest. The density of molecular lines is always very large, and it can be assumed that they are fully overlapped and/or weak. Frequency averaged models are nearly always employed in which only the bands within the system are considered individually (smeared band model) or only the gross shape of the band system itself is retained (bandless model). Such data is adequate for studies in which high spectral resolution is not required.

The low frequency band systems of the air species ($N_2(1+)$, $N_2(2+)$, $N_2^+(1-)$, $O_2(S-R)$, $NO(\beta)$, $NO(\gamma)$) have been extensively studied. Frequency averaged contributions are presented by Aroeste and Magee (Ref. 27) and Biberman and

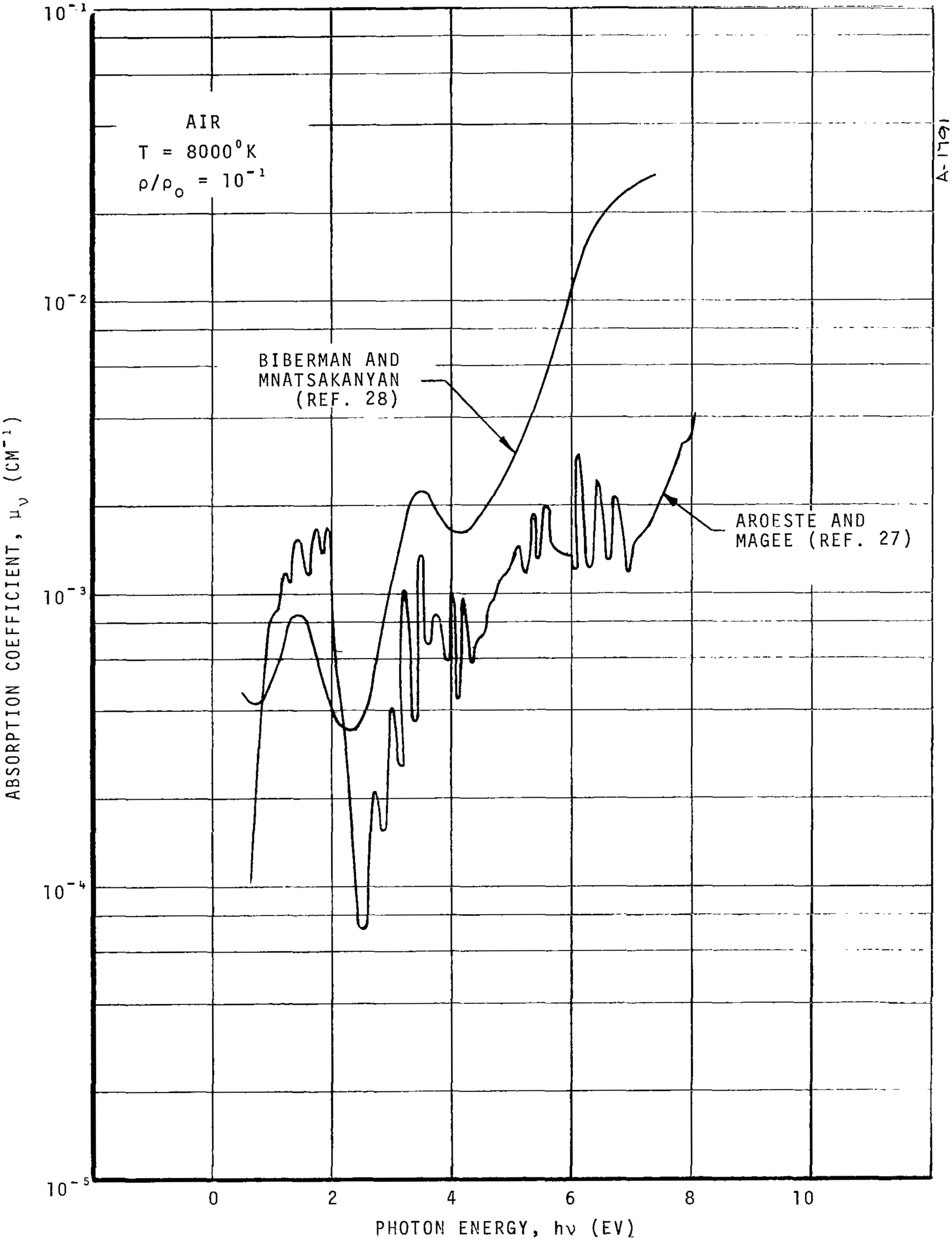

Figure 3. Typical Absorption Coefficient Predictions Including Important Molecular Contributions

Mnatsakanyan (Ref. 28), among others. A representative comparison* of their results is given in Figure 3. It is seen that noticeable differences exist in some of the details, but the general levels are in agreement except in the ultraviolet where Biberman and Mnatsakanyan (Ref. 28) included contributions from more transitions. Biberman and Mnatsakanyan (Ref. 28) showed that their data is also in good agreement with the data (viewed with low spectral resolution) of Churchill et.al. (Ref. 29) in which over 150,000 lines were considered individually.

A large number of high frequency band systems have been identified for the air species (see Ref. 30, for example). Sufficient data is not available to allow accurate calculations of the contributions from each individual band system; however, the total contribution from each molecular species can be estimated. Gilmore (Ref. 31) investigated the relative importance of O_2, NO and N_2 in air (contributions from other species being negligible), at $h\nu =$ 9.77 ev and for $2{,}000^\circ K \leq T \leq 8{,}000^\circ K$. He found that O_2, NO and N_2 contributions dominate at low, medium and high temperatures, in that order. The O_2 contribution was attributed to the usual photodissociation continuum. The sources of the NO and N_2 contributions have not been positively identified.

The high frequency contributions of NO were investigated by Biberman and Mnatsakanyan (Ref. 28). They found that the NO(δ) and NO(ε) systems make significant contributions in the range $5.2 \text{ ev} \leq h\nu \leq 8.2$ ev and for an extended range of temperature. At higher frequencies, the room temperature data of Watanabe (Ref. 32) show that important contributions from NO exist above $h\nu \approx 9.3$ ev. Biberman and Mnatsakanyan (Ref. 28) used the room temperature cross sections to estimate the high temperature contribution in this frequency range. The resulting total contribution for NO is high below 8.2 ev and above 9.3 ev with a pronounced minimum in between. This minimum is probably spurious, caused by a lack of data and the use of room temperature cross sections rather than an absence of absorbing mechanisms. Accordingly, Biberman and Mnatsakanyan (Ref. 28) recommend interpolating between the two contributions and disregarding the minimum. In view of the absence of more nearly complete data, this approach seems superior to the usual one of ignoring these systems.

The total high frequency contribution of N_2 has been investigated experimentally by Appleton and Steinberg (Ref. 33) and theoretically by Allen (Ref. 34).** In the experimental study, the contribution in the frequency range

---

[*] It was necessary to interpolate between the data points presented in Ref. 28 to allow the two sets of data to be compared.

[**] The contributions of particular band systems have also been studied by Churchill et.al. (Ref. 35) and Gilmore (Ref. 31).

$9.27 \text{ ev} \le h\nu \le 10.4 \text{ ev}$ are measured, and a method is suggested by which they can be obtained to 12.75 ev. In the theoretical study, Allen assumes that the total contribution is dominated by the long wave length "tail" of the N_2 Birge-Hopfield systems $b'\,{}^1\Sigma_u^+ - X\,{}^1\Sigma_g^+$ and $b\,{}^1\Pi_u - X\,{}^1\Sigma_g^+$ for the frequency range $7.0 \text{ ev} \le h\nu \le 14.25 \text{ ev}$. For frequencies above about 10.5 ev, the experimental data is substantially above the calculated data indicating that contributions from sources other than the Birge-Hopfield systems are important. However, there is no reason to believe that Allen's data is in error at the lower frequencies. Thus, the experimental data can be used in the frequency range $9.27 \text{ ev} \le h\nu \le 12.75 \text{ ev}$ and the theoretical data in the range $7.0 \text{ ev} \le h\nu \le 9.27 \text{ ev}$.

The contributions from the ablation product species are available from several sources. The species associated with the $CO_2 - N_2$ system have been studied by Arnold, Reis and Woodward (Ref. 36) and more recently by Woodward (Ref. 37). They considered the CN(V), CN(R), C_2 (Swan) and CO(4+) along with the usual air systems. The contribution from the first three band systems are considered to be reasonably well established. In the case of the CO(4+) system, significantly lower estimates of the magnitude of its contribution are also available (see Ref. 38, for example). The contributions of the C_2 (Freymark), C_2(Fox-Herzberg), C_2(Mulliken), H_2(Lyman) and H_2(Werner) band systems are also available (see Appendix A and Ref. 39).

3.1.4 Other Transitions

The O_2 Schumann-Runge photodissociation continuum is known to be the most important ultraviolet contributor for the air system at lower temperatures (Ref. 31). Evans and Schexnayder (Ref. 40) have studied this transition experimentally and numerically. A comparison between their results and the approximate Sulzer-Wieland formula

$$\mu_\nu^{PD} = 1.45 \times 10^{-17} \, N_i \left[\tanh\left(\frac{0.0975}{kT}\right)\right]^{1/2} \exp\left[-\tanh\left(\frac{0.0975}{kT}\right)\left(\frac{h\nu - 8.56}{0.805}\right)^2\right] \tag{53}$$

indicates that it is accurate up to temperatures sufficiently high to cause O_2 dissociation, provided that a threshold frequency of 7.1 ev is imposed.

The photodetachment transition of the negative ions of atomic oxygen and hydrogen are known to exist and to be important for some plasma conditions.

The cross sections for O^- are available from the work of Churchill, Armstrong and Mueller (Ref. 35). The cross sections of H^- are very well known and are available from several sources (Refs. 41, 42, and 43), agreement being on the order of five percent. The C^- ion is also known to undergo a photodetachment transition, and cross sections have been obtained by Cooper and Martin (Ref. 44), and are in fair agreement with the measurements of Seman and Branscomb (Ref. 45).

The contribution of the N^- ion is currently being debated. Norman (Ref. 46) argues in favor of an appreciable photodetachment contribution and points out that the utilization of a reasonable cross section ($\sim 8 \times 10^{-17} cm^2$) greatly enhances the agreement between calculated (Ref.15) and measured (Ref. 47) continuum emission. The recent measurements of Morris et.al. (Ref. 48) also indicates a substantial N^- contribution. However, the N^- contribution is not taken into account in most of the theoretical papers on the emission of an air plasma, including many of the most recent ones (Refs. 9, 14, and 19). It has not been positively established that the ion is stable, especially in its ground state. Further, its photodetachment cross section is completely unknown. Thus, the N^- photodetachment contribution is required to make predictions agree with recent experimental findings, but the transition is not sufficiently well understood to allow predictions to be made from first principles. A numerical investigation of the possible effects of this transition is given in Section 5.1.

The contributions from molecular photoionization transitions are important on occasion. Biberman and Mnatsakanyan (Ref. 28) found that the NO photoionization contribution makes an important contribution to their total high frequency NO contribution. However, other molecules such as CO, H_2, and O_2 have photoionization thresholds at such high frequencies that they can usually be neglected.

Finally, there is reason to believe that absorption and scattering by particulate matter (carbon primarily) can be important for some cases (see Ref. 38, for example). It is felt that this phenomena is not sufficiently well understood to be described quantitatively. Consequently, the present model is applicable to those cases where only a negligible interaction exists between the radiation field and any particulate matter.

3.2 THE RADIATION PROPERTIES MODEL

The radiation properties which are felt to be most nearly consistent with the objectives of the present study are given in Sections 3.2.1, 3.2.2, and 3.2.3. These are ultimately used in the numerical work presented in Section 5.

3.2.1 Molecular Band Model

The bands within each band system are smeared according to the scheme

$$\bar{\mu}_\nu = \frac{\int_{\Delta\nu} \mu_\nu d\nu}{\Delta\nu}$$

where the $\Delta\nu$ are selected such the $\bar{\mu}_\nu$ varies smoothly. The "bandless model" obtained in this fashion is essentially the same as that proposed originally by Meyerott et.al. (Ref. 49) and used more recently by Biberman and Mnatsakanyan (Ref. 28). It is felt to be satisfactory for radiation heating calculations.*

3.2.2 Atomic and Ionic Line Model

The line group approximation is employed to simplify the calculation. The frequency range of interest is divided into a number of frequency increments - 15 to 20 or thereabout. These are not necessarily connected. Each one defines as a line group those lines which are centered within it. The line contributions at a frequency point within a frequency increment is obtained by summing over only those lines within its group. This approximation is valid unless all three of the following conditions are satisfied:

(1) The path lengths are sufficiently long and the electron densities sufficient high to lead to blanketing.

(2) The line group boundaries are placed in between closely spaced lines.

(3) The continuum intensities are not already black body.

In addition, the line group approximation becomes inaccurate for extremely long path lengths where the equivalent width of an isolated line can become greater than the width of the line group.** The sketch illustrates the conditions where the line group approximation is valid (Figure 4(a)), introduces small errors (Figure 4(b)) and significant errors (Figure 4(c)).

---

*A discussion is given in Section 4.2 on the effect this approximate model has on the calculation of radiative fluxes.

**This very rarely occurs, however.

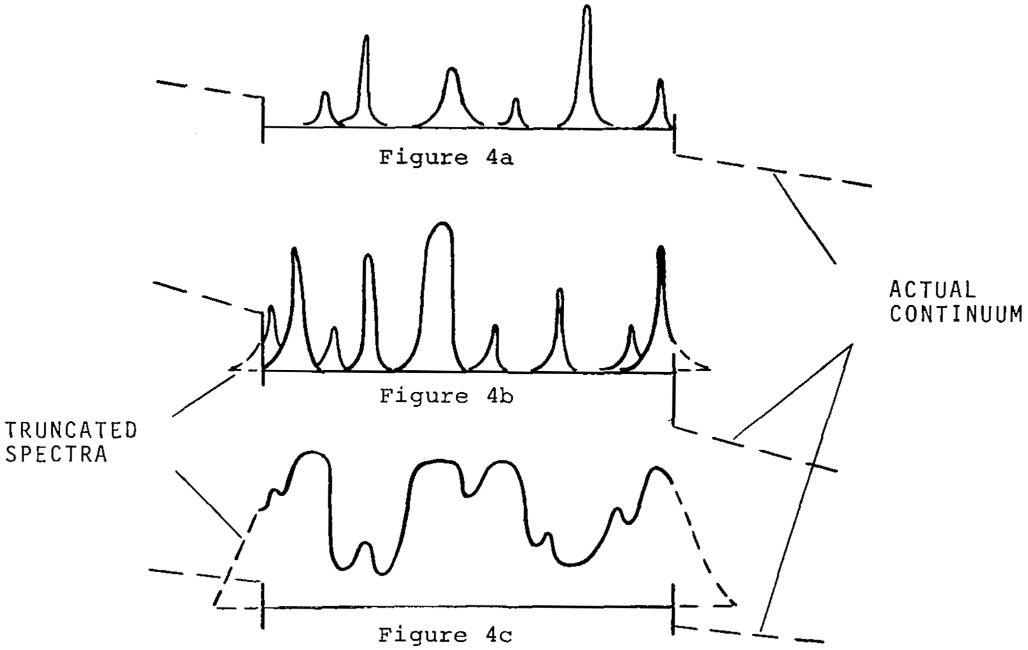

Figure 4. Intensities in the Line
Group Approximation

An additional classification of the lines is required. Lines having a lower level with a principal quantum number (n_L) of four or greater are considered to be high series lines. Contributions from them are obtained from integral formulas (Eq. (52)). Lines having an n_L equal to or less than two are the very strong lines situated in the ultraviolet. The contributions from them are calculated in full detail (within the line group approximation). Lines having an n_L of three appear in the infrared and, to a lesser extent, the visible range of the spectrum. They are of intermediate strength - probably too strong to be calculated by an integral formula but not strong enough to require a fully detailed calculation. Contributions from these lines are obtained by considering the contributions from an "average" line (defined by an averaged line width and f-number) and multiplying by the number of lines. The averaging process is limited to lines within the same line group and having lower levels with the same principal and orbital quantum numbers. This approach neglects line overlapping, an effect which should be of negligible importance for these lines for most cases of interest.

The radiative properties model adopted for the present calculations was taken from the sources of data given in Tables II-V. The atomic and ionic continuum contributions are given in Table II, the atomic and ionic lines in Table III the molecular bands in Table IV, and the other contributions in Table V.

TABLE II

ATOMIC AND IONIC CONTINUUM

Species	Transitions	Source
Hydrogen	High frequency photoionization edges	Eq. (36) with Gaunt factor of unity
	Low frequency photoionization	
	free-free	Eq. (38) with Gaunt factor of unity
Oxygen and Nitrogen	High frequency photoionization edges	Numerical data from Ref. 11
	Low frequency photoionization	Eq. (41) modified empirically to better agree with data from Ref. 11
	free-free	Eq. (38) with Gaunt factor of unity
Carbon	High frequency photoionization edges	Numerical data from Ref. 11
	Low frequency photoionization	
	free-frde	Eq. (38) with Gaunt factor of unity
All atomic ions	All transitions	Not included as their continuum transitions are negligibly small

TABLE III

ATOMIC AND IONIC LINES

		Sources of Data			
Species	Transitions	f-no.	Line Shape	$\frac{1}{2}$ width	Other
Hydrogen	Lyman α β Balmer α β	Ref.50	Numerical data from Ref.22	--	Eqs (46-48) used where applicable
	Other lines accounted for individually	Ref.50	Eq.(43)	Eq.(49)	Eq.(50) used when applicable
	High lines				Ionization threshold lowered $(\tilde{n} = 8)$
	High series				μ'_ν taken equal to j/B_ν with j from Eq. (52)
Oxygen Nitrogen Carbon (atoms and ions)	All lines accounted for individually	Ref.11	Eq.(43)	Ref.11 and Eq.(44)	Eqs. (45) and (50) used when applicable
	High lines				Ionization threshold lowered $(\tilde{n} = 8)$
	High series				μ'_ν taken equal to j/B_ν with j from Eq. (52)

TABLE IV

MOLECULAR BAND SYSTEMS

Species	Transitions	Source
N_2	1+ 2+	Curve fits to numerical data from Ref. 28
	Birge Hopfield	Curve fits to numerical data from Ref. 34 for $h\nu \leq 10.5$ ev and from Ref. 33 for $h\nu > 10.5$
O_2	Schumann-Runge Band System	Curve fits to numerical data from Ref. 28
NO	γ β ε,δ	
N_2^+	1-	
CN	red violet	Curve fits to numerical data from Ref. 37
C_2	Swan Freymark Mulliken	Curve fits to numerical data. See Appendix A.
H_2	Lyman Werner	
CO	4+	Curve fits to numerical data from Ref. 37

TABLE V

OTHER CONTRIBUTORS

Species	Transitions	Source
O_2	Photodissociation	Eq. (53)
O^-	Photodetachment	Curve fits to numerical data from Ref. 35
H^-	Photodetachment	Curve fits to numerical data from Ref. 41
N^-	Photodetachment	It is not included in the numerical work unless it is called out. Then, the contribution is consistent with the data of Ref. 48
C^-	Photodetachment	Numerical data from Ref. 45
N_2, O_2 CO, H_2 CN, C_2	Photoionization	Neglected
ALL	Particulate absorption and Scattering	Neglected
NO	Photoionization	Numerical data from Ref. 28

TRANSPORT MODEL

4.1 FORMULATION

The basic equation governing the transfer of radiation through a medium in local thermodynamic equilibrium can be written as

$$\frac{dI_\nu}{dS} = \mu'_\nu \left(B_\nu - I_\nu\right)$$

where I is the spectral intensity, B is the Planck function, S is the ray length, μ' is the absorption coefficient corrected for induced emission, viz.

$$\mu'_\nu = \mu_\nu \left[1 - \exp(-h\nu/kT)\right]$$

and μ_ν is the ordinary absorption coefficient.

In computing radiation fluxes across boundary and/or shock layers, it is convenient to make the tangent slab approximation. Thus, the properties along any ray can be related to those along the normal coordinate (y) by applying a cosine transformation. The coordinate system is shown in Figure 5. The resulting expressions for the optical depth, directional fluxes and total flux are well known and can be written in the form

$$\tau_\nu = \int_0^y \mu'_\nu dy \tag{54}$$

$$F^+_\nu(y) = \int_0^{\epsilon^+_b} E_\nu(\epsilon^+_\nu)\, d\epsilon^+_\nu \tag{55}$$

$$F^-_\nu(y) = \int_0^{\epsilon^-_b} E_\nu(\epsilon^-_\nu)\, d\epsilon^-_\nu + 2J^w_\nu \mathcal{E}_3(\tau_\nu) \tag{56}$$

$$q_r(y) = \int_0^\infty \left[F^+_\nu(y) - F^-_\nu(y)\right] d\nu \tag{57}$$

where a diffuse wall has been assumed (reflectance r^w_ν and emittance ϵ^w_ν) and where E_ν and J^w_ν are the black body emissive power and wall radiosity, respectively, and are defined as

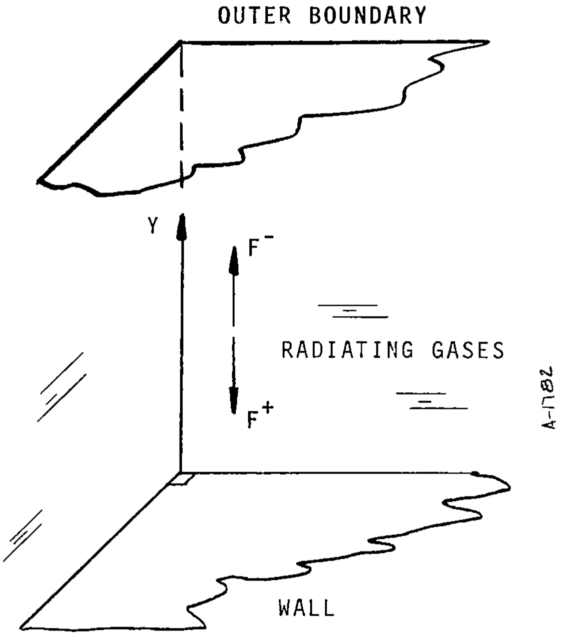

Figure 5. Coordinate System

$$E_\nu = \pi B_\nu \tag{58}$$

$$J_\nu^w = \varepsilon_\nu^w E_\nu(0) + r_\nu^w F_\nu^+(0) \tag{59}$$

Finally, emissivities ($\varepsilon_\nu^\pm$) are used as independent variables,

$$\varepsilon_\nu^+ = 1 - 2\mathscr{E}_3(t_\nu - \tau_\nu)\ ,\ t_\nu \geq \tau_\nu \tag{60a}$$

$$\varepsilon_\nu^- = 1 - 2\mathscr{E}_3(\tau_\nu - t_\nu)\ ,\ t_\nu \leq \tau_\nu \tag{60b}$$

where the t_ν are dummy values of optical depth and the $\mathscr{E}_n(x)$ functions are exponential integrals of order n.

The exponential approximation can be used to further simplify the equations without an appreciable loss in accuracy. It is known (see Ref. 9, for example) that when the approximation

$$2\mathscr{E}_3(x) \approx \exp(-2x) \tag{61}$$

is made, exact transport solutions are obtained in the optically thin limit, viz.

$$F_\nu^\pm(\tau_\nu) = 2\int_{|t_\nu^b - \tau_\nu|} E_\nu(t_\nu)dt_\nu\ , \qquad \tau_\nu^b \to 0 \tag{62}$$

In the optically thick limit, the directional fluxes become

$$F_\nu^\pm = E_\nu \pm \frac{C}{\mu_\nu}\frac{\partial E_\nu}{\partial y} + \ldots\ O\left(\frac{1}{\mu_\nu^2}\right), \qquad \mu_\nu \to \text{large} \tag{63}$$

where C = 1/2 for the approximate model and 2/3 for the exact model. Thus, the approximate model agrees through the first term (hence it is exact in the limit $\mu_\nu \to \infty$). Further, the net flux as calculated from the Rosseland formula, viz.

$$F_\nu^+ - F_\nu^- = \frac{2C}{\mu_\nu}\frac{\partial E_\nu}{\partial y} + \ldots\ O\left(\frac{1}{\mu_\nu^3}\right) \tag{64}$$

is of satisfactory accuracy considering its higher order nature, viz.

$$F_\nu^+ - F_\nu^- \to 0 \text{ as } \mu_\nu \to \infty$$

Thus, the emissivities become

$$\varepsilon_\nu^+ \approx 1 - \exp 2(\tau_\nu - t_\nu) \tag{65a}$$

$$\varepsilon_\nu^- \approx 1 - \exp 2(t_\nu - \tau_\nu) \tag{65b}$$

which are more convenient to work with than those given by Equations (60a) and (60b). Emissivities written in this form have the additional advantage that by suppressing the factor of 2 in the exponential arguments and replacing E by B in Equations (56) and (57), the same formulation can be used to calculate intensities.

Before evaluating Equations (54)-(57) it is advantageous to separate the integrals into line and continuum parts. This allows optimum coordinates to be selected in frequency space. The continuum contribution to the absorption coefficient ($\equiv \mu_\nu^C$) is just the first term in Equation (34). Substituting μ_ν^C for μ_ν in Equations (54)-(57) yields corresponding values for τ_ν^C and F_ν^C, where the $\pm$ signs have been dropped from the latter for brevity. The line contributions to the flux are obtained by difference

$$F_\nu^L \equiv F_\nu - F_\nu^C \tag{66}$$

where the F_ν values are evaluated using the total absorption coefficient (Eq.(34)). Thus, the line contribution is treated as a correction to the continuum flux.*

4.2 EVALUATION OF FLUX INTEGRALS

A direct evaluation of Equations (54)-(57) requires an implicit assumption - that only a reasonable number of frequency points need be sleected to adequately describe the variation of the spectrum. In the case of the continuum spectrum, the assumption is well satisfied with about 25-50 points being sufficient. In the case of atomic lines, the number is approximately 1,000 frequency points (100 lines with 10 points per line), which is getting large but can still be handled for most cases. In the case of molecular lines the requirement rises to approximately 1,500,000 frequency points (150,000 lines with 10 points per line), which is quite impractical for radiation heating calculations.

---

*It should be noted that the line contributions defined by Equation (66) can be negative for nonisothermal layers.

In the present study, the problem of resolving the molecular spectrum is solved summarily. The utilization of the molecular band model (the bandless model) converts the molecular spectrum into an "equivalent" continuum process. Such an approach ignores the details of the internal structure of the band system. The calculated spectral fluxes yield the correct total fluxes (when integrated over a band system) only when the layer is optically thin, optically thick, or when the lines are spaced sufficiently close together to be strongly overlapped. Otherwise, only an approximation to the total flux is obtained.*

No additional approximations are required. The continuum fluxes and the approximation to the molecular line fluxes can be calculated in a straightforward manner. The atomic and ionic line fluxes can also be obtained directly. While this calculation is lengthy, it is not felt to be excessively so. In all cases careful attention must be paid to the selection of nodal points (in frequency and in space) and interpolation formulas to insure that high accuracy is maintained.

4.2.1 Nodal Points in Frequency

For the continuum contribution to the flux integrals the frequency grid can be specified _a priori_ and is only slightly dependent on the characteristics of the layer. Basically, the variation of the Planck function and the continuum absorption coefficients must be adequately described. The first requirement can be met by distributing nodal points across the frequency range $h\nu \approx 0.25$ ev to $h\nu_{max} \approx 12\ kT_\infty$ ev (T_∞ = maximum temperature considered). Usually about 30 points spaced at roughly equal intervals are sufficient. This grid also satisfies the second requirement except in the ultraviolet.

---

* The accuracy of the approach can be defended on the following grounds: (1) The molecular spectra for which good property data are available are all situated in the infrared, visible, or near ultraviolet. It is well known that this region of the spectrum is optically thin for typical boundary or shock layer conditions and, hence, the bandless model is accurate for these data. (2) The molecular spectra situated in the ultraviolet and the vacuum ultraviolet are often strong enough to absorb appreciably. However, good radiation property data are not available in this region; consequently, the bandless model approach is consistent with the quality of the data. (3) Finally, and of primary importance, it is known that whenever radiation heating is comparable to convective heating, the molecular species will be confined to a narrow layer near the wall. The radiation will originate in the external region of the flow which will be hot enough to be dissociated and at least partially ionized. Thus, in any competition for accuracy and/or detail the atom and ion radiation must be given preferential treatment.

It is to be noted that more sophisticated band models are used by some investigators. These extend the range of validity somewhat, but introduce what is basically the same type of approximation and are accurate in the same regimes.

There the frequency grid must be carefully selected to resolve the photoionization thresholds.*

For the line contribution to the transport integrals, a grid must be selected for each line and should be dependent upon the characteristics of the layer as well as the individual line. This is accomplished by introducing a parameter φ which is characteristic of the width of the line (and will be discussed further in a subsequent paragraph) to stretch the coordinate system. The smallest increment and the distance to the most remote nodal point are defined by Equations (67) and (68), respectively, where $\tilde{\nu} = |\nu - \nu_c|$.

$$\delta\tilde{\nu}_o = f_1\varphi \tag{67}$$

$$\tilde{\nu}_{max} = f_2\varphi \tag{68}$$

The quantities f_1 and f_2 are selected arbitrarily and are usually taken to be 0.5 and 10 (respectively), on this order. The intermediate nodal points are established using a growth law, viz.

$$\delta\tilde{\nu}_j = (1 + f)\ \delta\tilde{\nu}_{j-1} \tag{69}$$

where the nodal spacing increases (increasing subscript j) with increasing distance from the center of the line. The growth factor f is determined implicitly from the relation

$$\tilde{\nu}_{max} = \frac{(1 - f)^N - 1}{f}\ \delta\tilde{\nu}_o \tag{70}$$

where N is the number of increments to be used. Usually, the center of the line and about 5 to 7 additional points in each direction from it are sufficient.

The stretching parameter φ is defined by Equation (71),

$$\varphi \equiv \gamma(\bar{y})\sqrt{1 + \tau_c} \tag{71}$$

where the (half) half width $\gamma(\bar{y})$ is evaluated at a particular spatial location (usually as an edge condition) and τ_c is the optical depth of the entire layer

---

*It should be noted that the movement of the thresholds (in frequency) caused by plasma interaction effects is not considered. This is consistent with the approximation discussed in Section 3.

at the frequency of the center of the line. It can be shown that φ has the following properties:

$$\lim_{\tau_c \to 0} \varphi = \gamma(y) \tag{72}$$

$$\lim \varphi \approx h\tilde{\nu}\Big|_{\tau_{\tilde{\nu}} = 1}$$

$$\gamma(\bar{y}) / \left[h\tilde{\nu}\Big|_{\tau_{\tilde{\nu}}=1} \right] \to 0 \tag{73}$$

That is, the φ is the distance in frequency space from the center of the line to the half intensity position when the line is weak, and it is approximately the distance to the frequency at which the layer has unit optical depth when the line is strong. At intermediate values of τ_c, φ should also be a reasonable approximation to the width of the line.

4.2.2 Nodal Points in Space

Initially a spatial grid is selected so that it adequately describes the variations of the thermodynamic properties across the radiating layer (the circles shown in Figure 6, for example). The optical depths are then calculated* and used to evaluate the emissivities. Typical values are shown in Figure 6(b) where Curves 1, 2 and 3 illustrate the optically thin, moderately thick and very thick layers, respectively. Transforming into the E_ν vs. ε_ν plane yields the points shown (as circles) in Figure 6(c). Curves 1 and 2 are well-behaved; however, Curve 3 is very ill-behaved, showing a discontinuity in slope at the outer boundary and no resolution of the region between the boundaries. To circumvent the problems caused by this behavior, a special

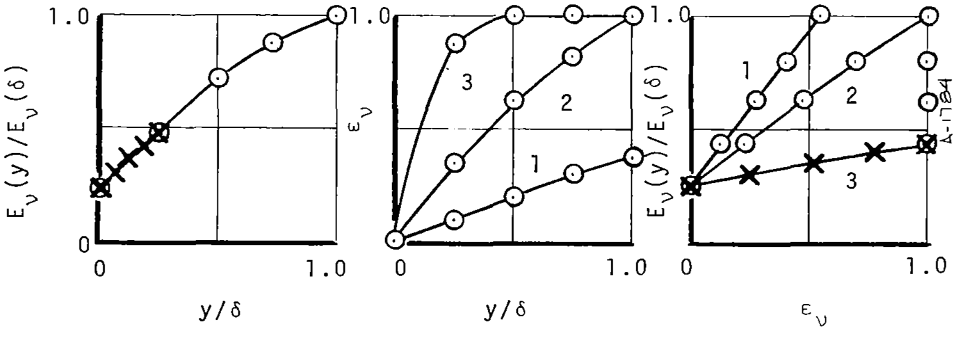

(a) (b) (c)

Figure 6. Spatial Grid Transformations

---

[*] The methods used to evaluate the integrals appearing in Equations (55)-(58) will be described subsequently.

coordinate system is used for the optically thick layers ($\tau_\nu > 2$ for present purposes). The layer is divided into equal increments of emissivities (crosses in Figure 6(c) from which the new values of optical depth are calculated.* The new E_ν values are then obtained by cubic interpolation in the plane $\ln E_\nu$ vs. $\ln \tau_\nu$.** The new curve in the E_ν vs. ε_ν plane (crosses in Figure 6(c)) is suitable for accurate evaluation by numerical methods.

4.2.3 Integration Scheme

With one exception, all the integrals are evaluated using three term Taylor's series expansions as interpolation formulas. The derivatives required in the second two terms are obtained from Equation (74), where x and y are the general independent and dependent variables, respectively.

$$\frac{dy}{dx} = ys \tag{74}$$

The s values are taken equal to the slopes in the plane ln y vs. x and are obtained from curve fits. It has been found that this procedure minimizes unwanted excursions in the higher order terms.

The Taylor's series expansions cannot be used for the frequency integration of the continuum fluxes due to the discontinuities in the integrals. These integrals were evaluated using linear interpolation formulas, instead. This causes no serious loss in accuracy as the integrals are slowly varying except at the discontinuities.

4.2.4 The Optically Thick Limit, An Example

Consider a radiation layer which has an overall optical depth of μL, a black body emissive power of E_{b_ν} at its midpoint and a constant gradient across the layer given by the relation

$$\frac{dE_{b_\nu}}{d\tau} = \frac{CE_{b_\nu}}{\mu L}$$

---

*In evaluating the optical depths, the maximum allowable value of ε_ν is taken to be 0.99.

**The origin of the optical depth integration is shifted and/or inverted in space to insure that the $\ln E_\nu$ vs. $\ln \tau_\nu$ curve is well behaved for the interpolation.

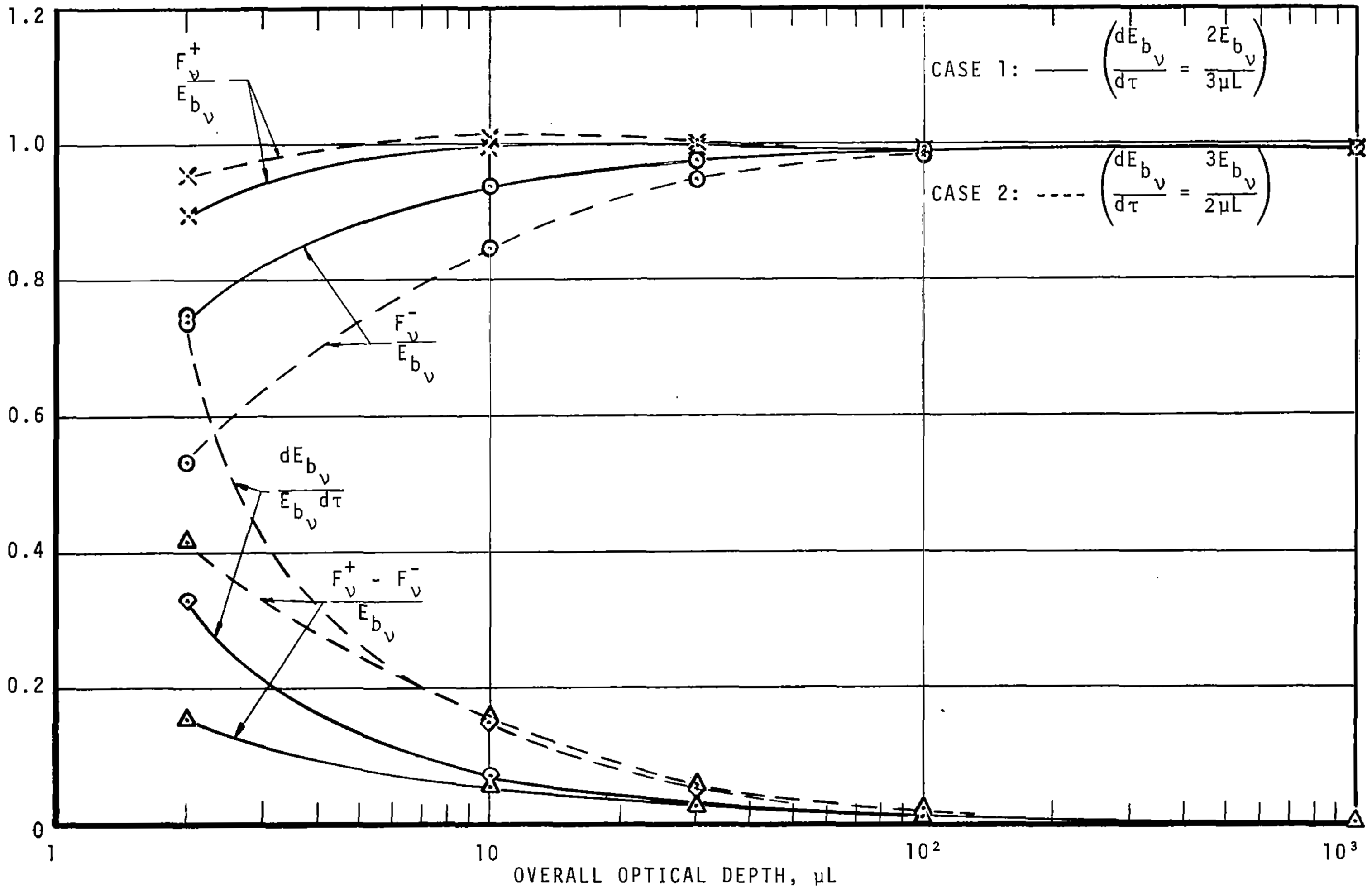

Figure 7. The Spatial Integrals in the Optically Thick Limit

The directional and net fluxes at the midpoint have been calculated using the methods of Sections 4.2.2 and 4.2.3. Values of C of 2/3 and 3/2 were selected, and the calculation was performed as a function of μ while holding L and E_{b_ν} fixed. The results are presented in Figure 7. The directional fluxes were driven to their correct limit (black body) by $\mu L \simeq 10^2$. Likewise, the net flux was driven to the gradient of the black body emissive power (correct within the constraints of the exponential approximation) by $\mu L \simeq 10^2$. This demonstrates that the methods of Sections 4.2.2 and 4.2.3 remain valid in the optically thick limit.

4.3 THE ADVANCED RADIATION TRANSPORT PROGRAM (RAD/EQUIL)

The entire solution procedure has been programmed for the CDC 6600. A description of the program has been presented elsewhere (Ref. 51). Typically, about 30 seconds of computer time are required to calculate the flux from the boundary of a uniform layer.

SECTION 5

APPLICATION OF THE METHOD

A matrix of theoretical predictions has been obtained. These are compared with predictions from other studies in Sections 5.1 and 5.2 and with experimental data in Section 5.3. Calculations of the radiative transport through isothermal layers are given in Section 5.4 and through a nonisothermal layer in Section 5.5, both as examples of the use of the prediction method.

5.1 COMPARISON WITH OTHER PREDICTIONS OF THERMODYNAMIC VARIABLES

The first set of theoretical predictions is given in Tables VI and VII and Figure 8. The temperatures and pressures specified in Table VI were used to predict densities, enthalpies and entropies for comparison with the results of Gilmore (Ref. 7) and Hilsenrath and Klein (Ref. 52) and mole fractions for comparison with the results of Armstrong and Scheibe (Ref. 53) and Hilsenrath and Klein (Ref. 52). The specified conditions of Table VI correspond to density ratios of 10^{-1}, 10^{-2} and 10^{-3} from Reference 52, and will hereafter be referred to as the nominal density ratios ($\rho/\rho_o(N)$). The density ratios agree to within approximately 1 percent (Table VI), the enthalpies to within approximately 3 percent (Table VII and the entropies to within approximately 2 percent (also Table VII). The mole fractions agree to within 10 percent, generally (Figure 8), except for O^- where the results of Hilsenrath and Klein (Ref. 52) appear to be high. Differences of this order can be attributed to the thermochemical data, the consideration of pressure dependent partition functions (in Ref. 7) and the consideration of nonideal gas effects (in Ref. 52).

TABLE VI

AIR PRESSURES AND DENSITIES

T (^0K)	Pressure (atm)			$(\rho/\rho_o)/(\rho/\rho_o(N))$		
	$\rho/\rho_o(N) = 10^{-3}$	$\rho/\rho_o(N) = 10^{-2}$	$\rho/\rho_o(N) = 10^{-1}$	$\rho/\rho_o(N) = 10^{-3}$	$\rho/\rho_o(N) = 10^{-2}$	$\rho/\rho_o(N) = 10^{-1}$
8,000	0.0586	0.564	4.915	1.010	1.012	1.012
9,000	0.0676	0.657	6.17	1.008	1.010	1.013
10,000	0.07909	0.747	7.196	1.007	1.009	1.012
11,000	0.0948	0.850	8.115	1.002	1.007	1.011
12,000	0.1161	0.979	9.066	0.997	1.005	1.010
13,000	0.1421	1.140	10.13	0.992	1.000	1.008
14,000	0.1699	1.339	11.35	0.991	0.996	1.005
15,000	0.1959	1.568	12.78	0.992	0.992	1.002

TABLE VII

AIR ENTHALPIES AND ENTROPIES

T (^{0}K)	h/RT			S/R		
	Present* Calculation	Hilsenrath and Klein	Gilmore	Present Calculation	Hilsenrath and Klein	Gilmore
	$\rho/\rho_o = 10^{-3}$ (nominal)					
8,000	18.03	18.40		60.55	61.21	
9,000	17.78	18.16		62.11	62.82	
10,000	18.74	19.07	19.08	64.65	65.35	65.31
11,000	21.21	21.40	21.43	68.60	69.19	69.10
12,000	24.96	24.95	25.00	73.85	74.24	74.07
13,000	29.11	28.92	28.04	79.59	79.79	79.51
14,000	32.45	32.23	32.25	84.65	84.81	84.39
15,000	34.30	34.14	34.14	88.31	88.52	88.00
	$\rho/\rho_o = 10^{-2}$ (nominal)					
8,000	16.76	17.14		54.82	55.49	
9,000	16.61	17.03		56.35	57.09	
10,000	16.40	16.84	16.84	57.62	58.42	58.42
11,000	16.78	17.20	17.22	59.30	60.13	60.11
12,000	17.90	18.25	18.29	61.62	62.42	62.38
13,000	19.74	19.99	20.05	64.62	65.33	65.26
14,000	22.11	22.22	22.30	67.13	68.72	68.60
15,000	24.66	24.60	24.69	71.83	72.28	72.10
	$\rho/\rho_o = 10^{-1}$ (nominal)					
8,000	13.02	13.35		47.18	47.76	
9,000	14.80	15.25		50.22	50.95	
10,000	15.14	15.63	15.64	51.86	52.67	52.68
11,000	15.06	15.56	15.57	52.98	53.85	53.85
12,000	15.11	15.60	15.63	54.11	55.02	55.02
13,000	15.46	15.94	15.99	55.45	56.39	56.39
14,000	16.16	16.61	16.69	57.07	58.00	58.02
15,000	17.18	17.57	17.69	58.97	59.88	59.90

*A correction of 129 Btu/lb has been added to the tabulated enthalpies to correct for the differences in base state. Also, a value of

$$R = 6.8610 \times 10^{-2} \text{ Btu/lb}^0\text{R}$$

was employed in the present study.

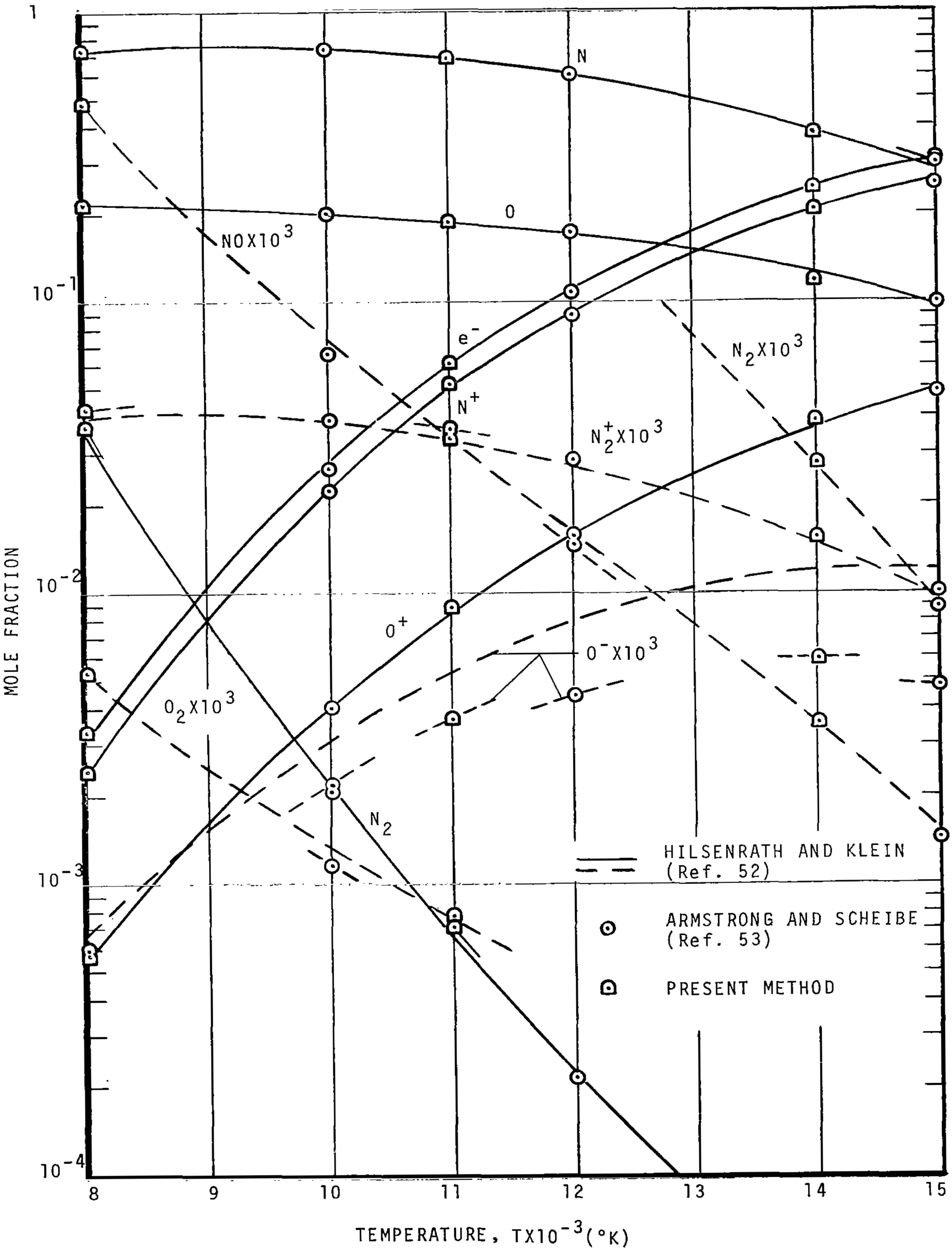

Figure 8. Mole Fractions of Air, $\rho/\rho_o = 10^{-2}$

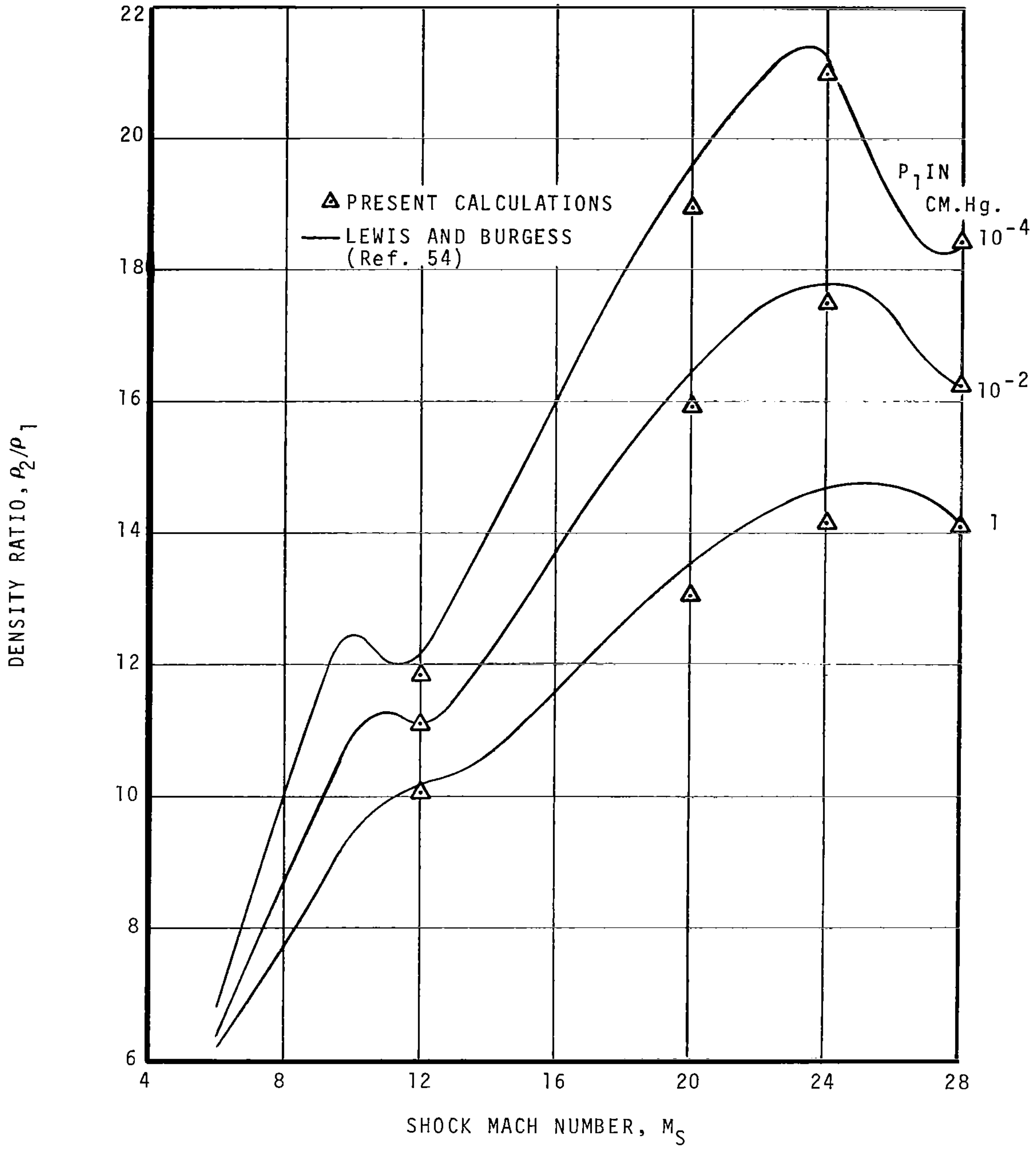

Figure 9. Shock Density Ratios for Air

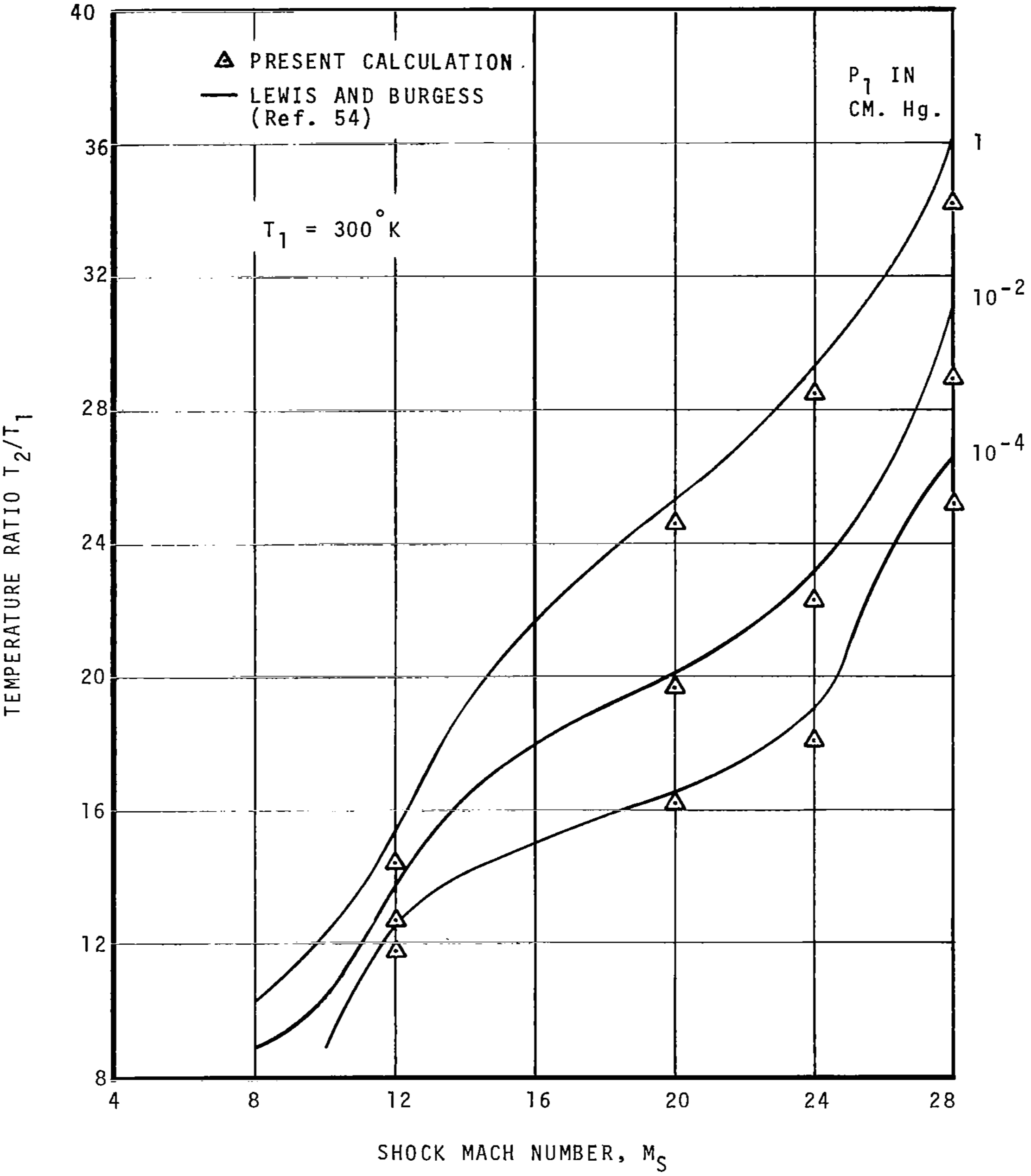

Figure 10. Shock Temperature Ratios for Air

The second set of predictions is presented in Figures 9 and 10 for the density and temperature ratios, respectively, across normal shock waves in air. The predictions are compared with data from the study by Lewis and Burgess (Ref. 54). The differences are approximately 4 percent for the density ratios and 5 percent for the temperature ratios. These are not inconsistent with the differences observed previously between the present predictions and those of Hilsenrath and Klein (Ref. 52), whose data was used by Lewis and Burgress (Ref. 54).

The final set of predictions of thermodynamic variables is presented in Figures 11 and 12 for the density and temperature ratios, respectively, across normal shock waves in a proposed Martian atmosphere (65% CO_2, 35% A by volume). The predictions are compared with data from the study by Heron (Ref. 55). The differences are approximately 2-1/2 percent for the density ratios and 3 percent for the temperature ratios, both readily attributable to small differences in the thermochemical data.

5.2 COMPARISON WITH OTHER PREDICTIONS OF RADIATIVE TRANSPORT

The first set of theoretical predictions is given in Figure 13 and compared with the semi-empirical predictions of Morris et.al. (Ref. 48). Three predictions are presented using the present model - one without an N^- contribution, one with an N^- contribution and a cross section of 8 x 10^{-17} cm^2 as suggested by Norman (Ref. 46), and one with an N^- contribution and a cross section of 1.6 x 10^{-16} cm^2 which makes the present predictions agree with the predictions of Morris et.al. (Ref. 48). While a cross section of 1.6 x 10^{-16} cm^2 is larger than that of most continuum transitions, it is neither so large nor so different from the one suggested by Norman (Ref. 46) as to appear to be unreasonable. However, based on this evidence alone, it cannot be concluded that the present predictions are consistent with those of Morris et.al. (Ref. 48).

Additional predictions of the nitrogen continuum intensities are given in Figure 14 and compared with the predictions of Biberman and Norman (Ref.15) and with the data of Boldt (Ref. 47) and Morris et.al. (Ref. 48). It is seen that the present predictions (without N^-) are greater than those by Biberman and Norman (Ref.15) by about a factor of two;* likewise, the measurements of Morris et.al (Ref. 48) are greater than the measurements of Boldt et.al. (Ref.

---

*In this spectral region, the absorption coefficients used by Biberman and Norman (Ref.15) dip below those used in the present study; otherwise, the agreement is generally very good.

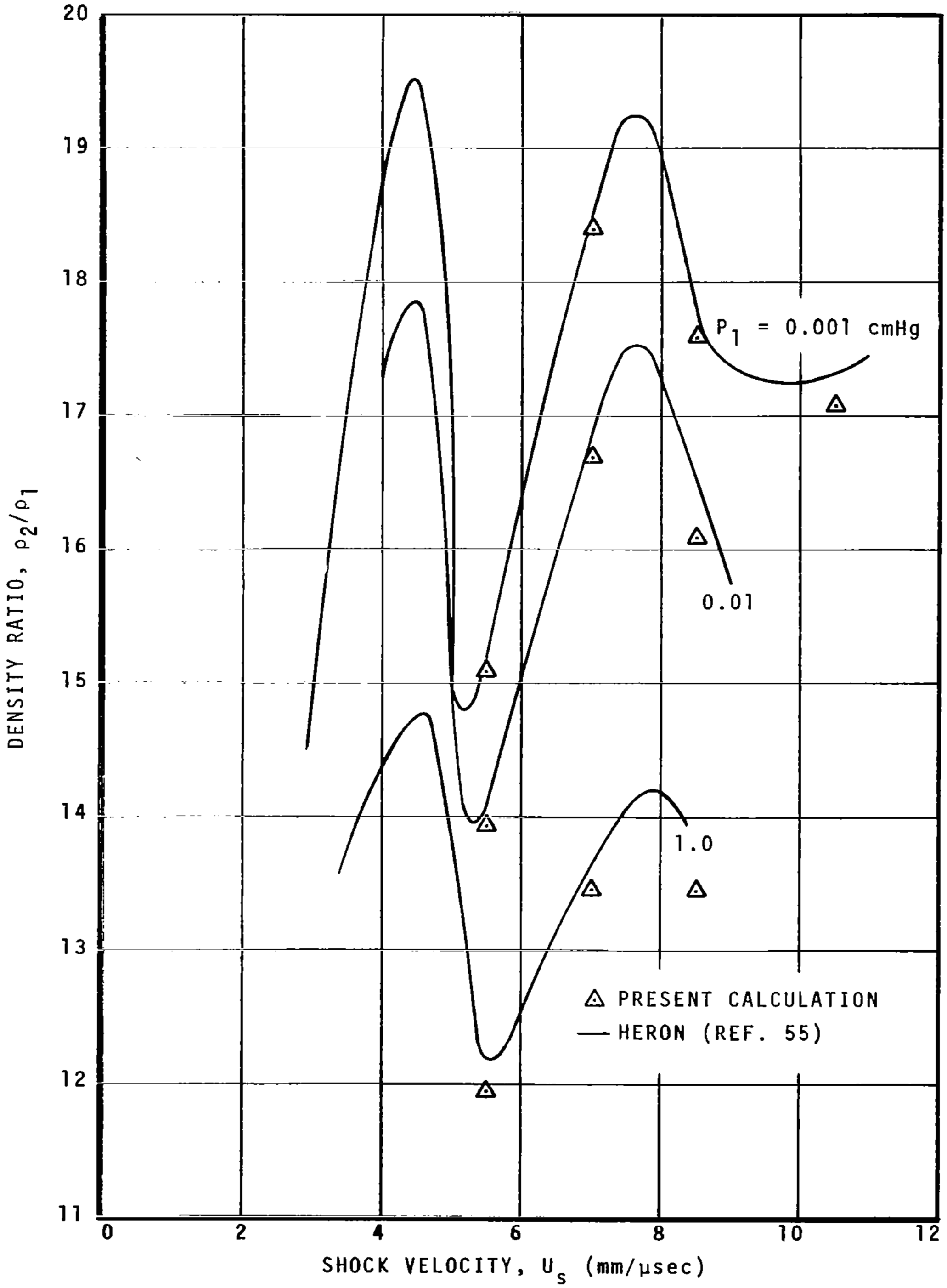

Figure 11. Shock Density Ratios for a Proposed Martian Atmosphere

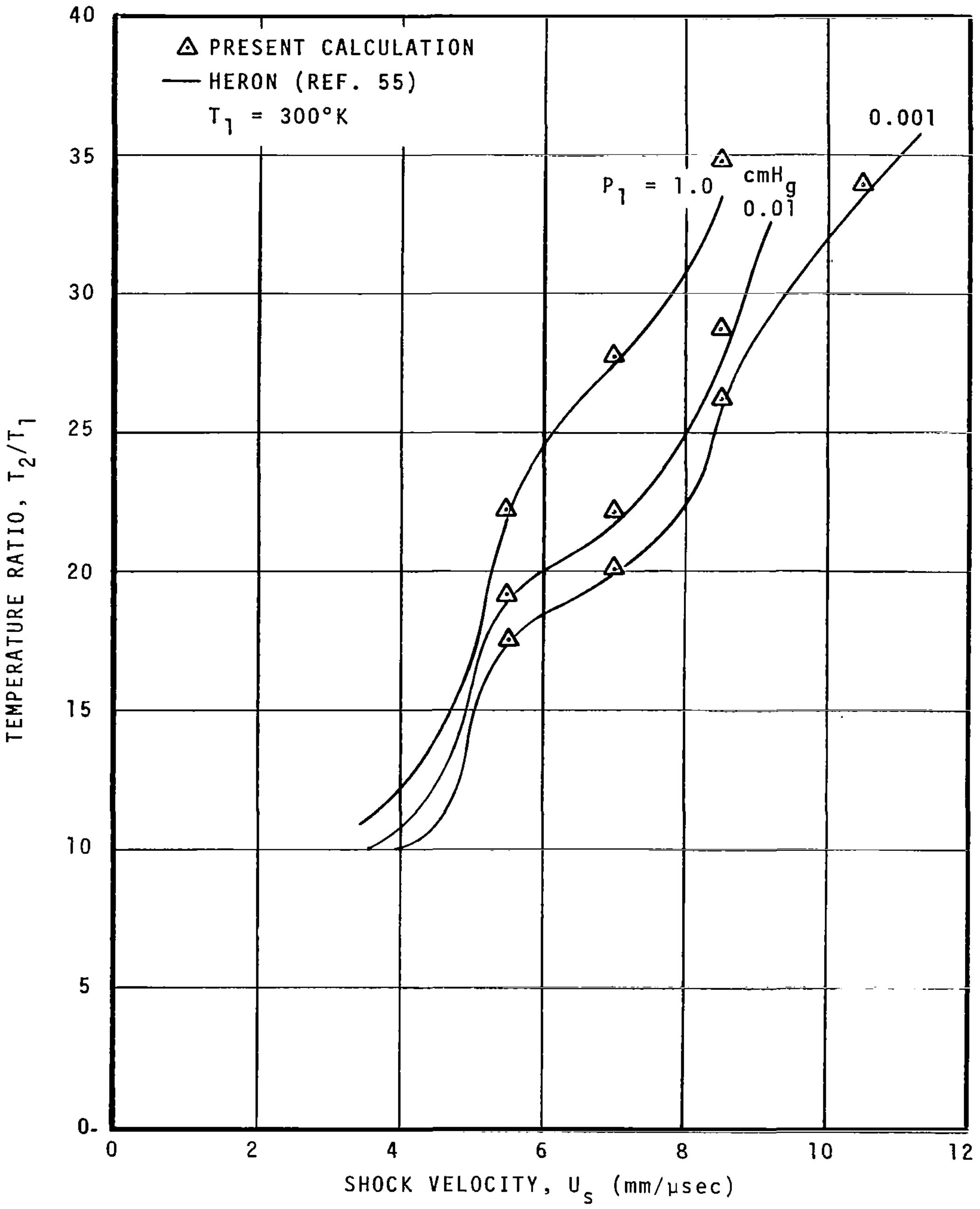

Figure 12. Shock Temperature Ratios for a Proposed Martian Atmosphere

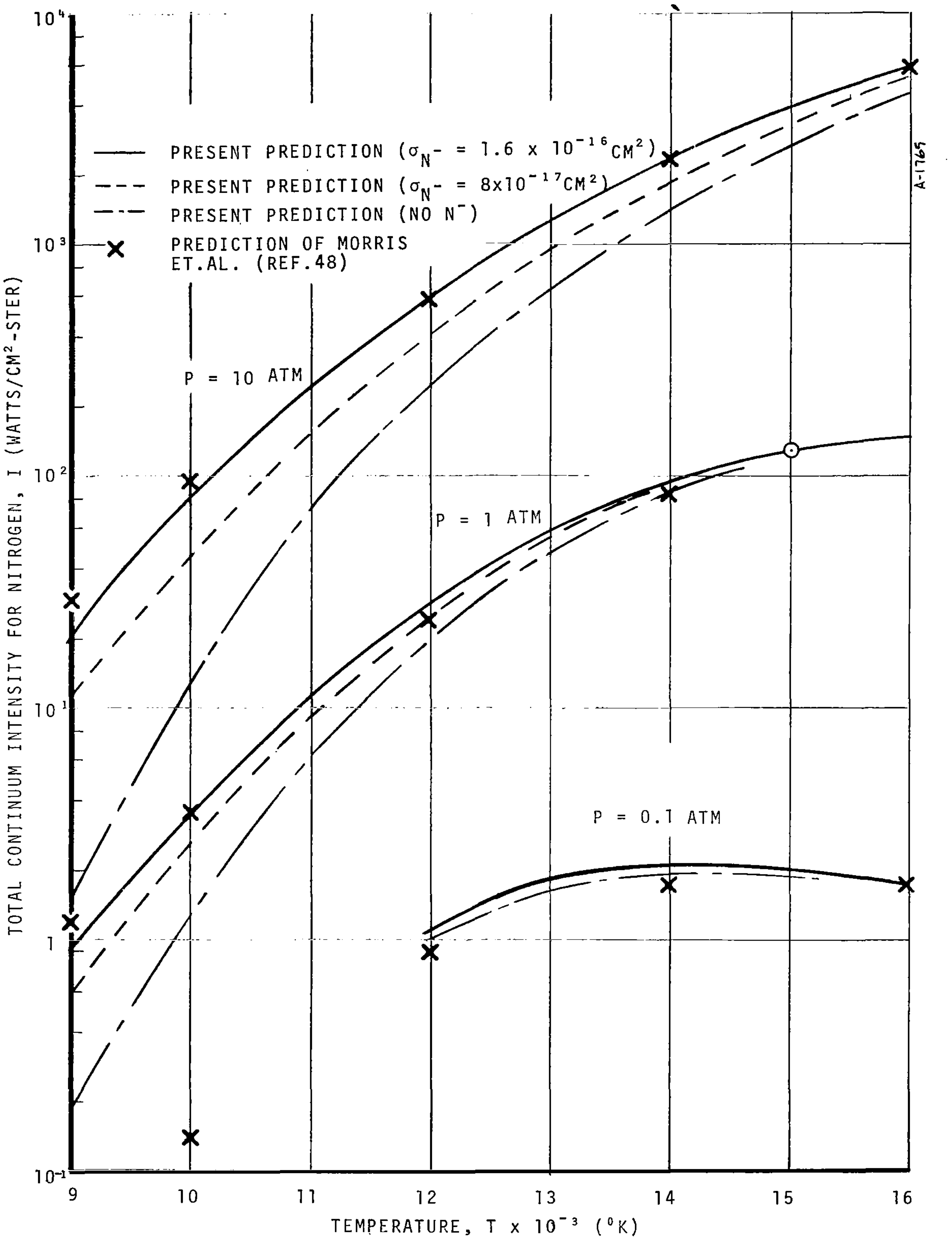

Figure 13. Comparison with the Predictions of Morris et al. (Ref. 48)

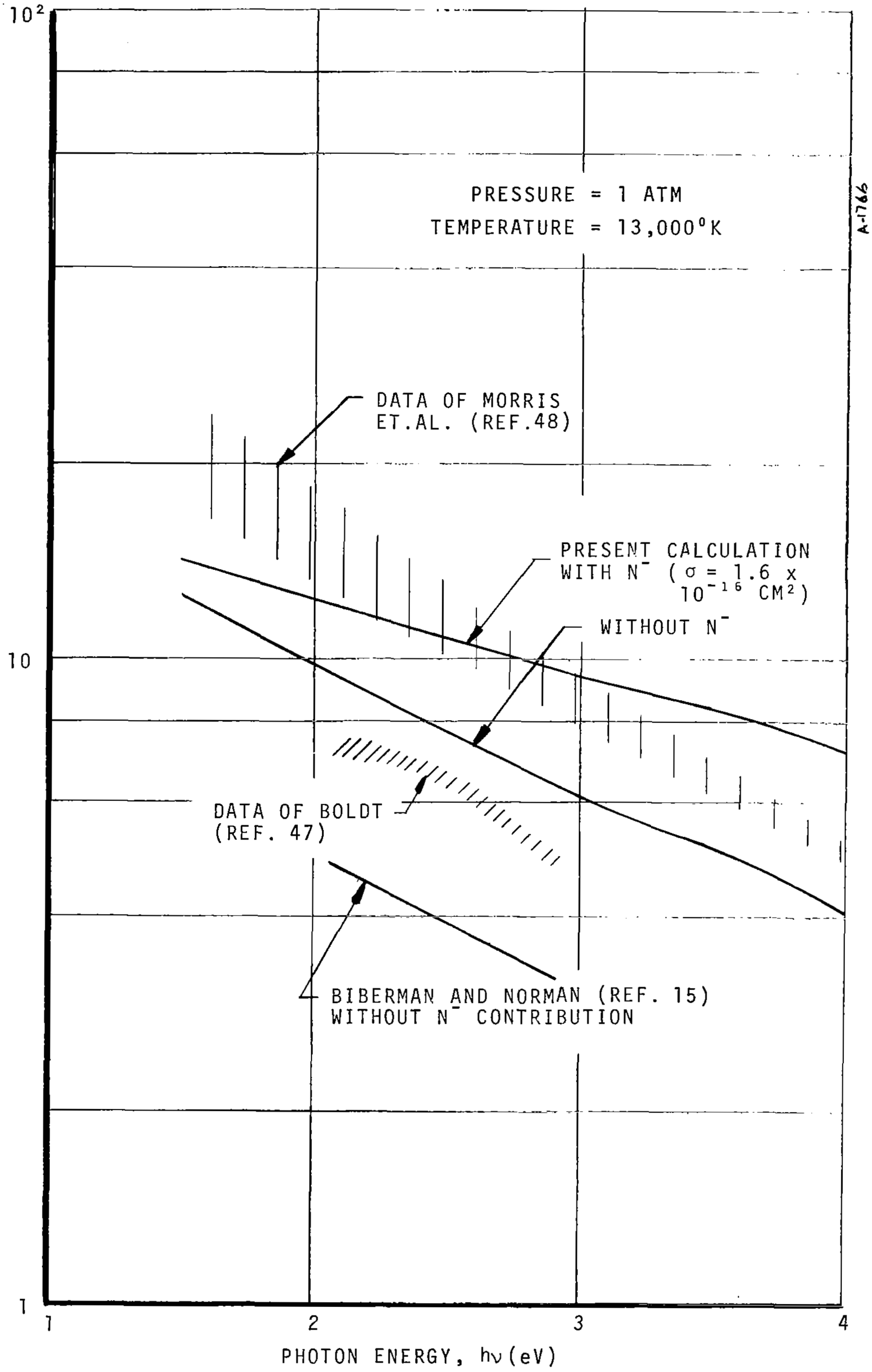

Figure 14. Effect of N^- on the Spectral Distribution of the Intensity of Nitrogen, δ = 1 cm

47) by about a factor of two. Thus, assigning the difference between measurement and prediction to the N^- contribution can yield either the rough agreement noted previously or gross differences in the N^- cross section, depending on the combinations of measurements and predictions selected. It is also seen in Figure 15 that the present predictions (without N^-) are in fair agreement with both sets of measurements and that the slopes of all the predictions (without N^-) are in good agreement. The agreement in slope is destroyed when the N^- contribution is included in the present predictions. Thus, forcing agreement between the present predictions and the total intensities predicted by Morris et al. (Ref. 48) decreases the agreement between the predictions and their spectral data.

In a more recent study, Morris et al. (Ref. 56) measured the continuum contributions between the atomic lines and molecular band systems to obtain a frequency dependent cross section for N^-. The interpretation of their measurements was not unambiguous;* nevertheless, this study considerably strengthened the case for an important N^- contribution. In the numerical work to be presented subsequently, their cross section is employed when an N^- contribution is called out (Figure 13 excepted). When an N^- contribution is not called out, it is not included.

The theoretical predictions for air are presented in Figure 15 and compared with the theoretical predictions of Wilson and Greif (Ref. 19). Their properties model for the atomic and (positive) ionic species is very similar to that used in the present study (Ref.11). However, they did not include contributions from the molecular species or the negative ions. In addition, they employ the effective width approach which approximates the contributions due to the atomic and ionic lines. The resulting predictions (Fig.15) are in excellent agreement for the $\delta = 1$ cm case except at the lower temperatures where the molecular contributions are clearly important. For the $\delta = 10$ cm case, the predictions differ by about 25 - 35 percent, even in the temperature range where no differences should exist. This difference cannot be attributed to fundamental differences in either the properties or the transport models. Molecular contributions are negligible above about $T \approx 12{,}000^\circ K$. In addition, the differences in calculating line effects cannot be responsible as they would be in the opposite direction. However, Wilson and Greif (Ref. 19) utilize Equation (41) as a convenient approximation to the continuum absorption

---

*The overlapped region between the atomic lines of N and O and the bands of the $N_2^+(1-)$ band system could have obscured the actual continuum conbribution.

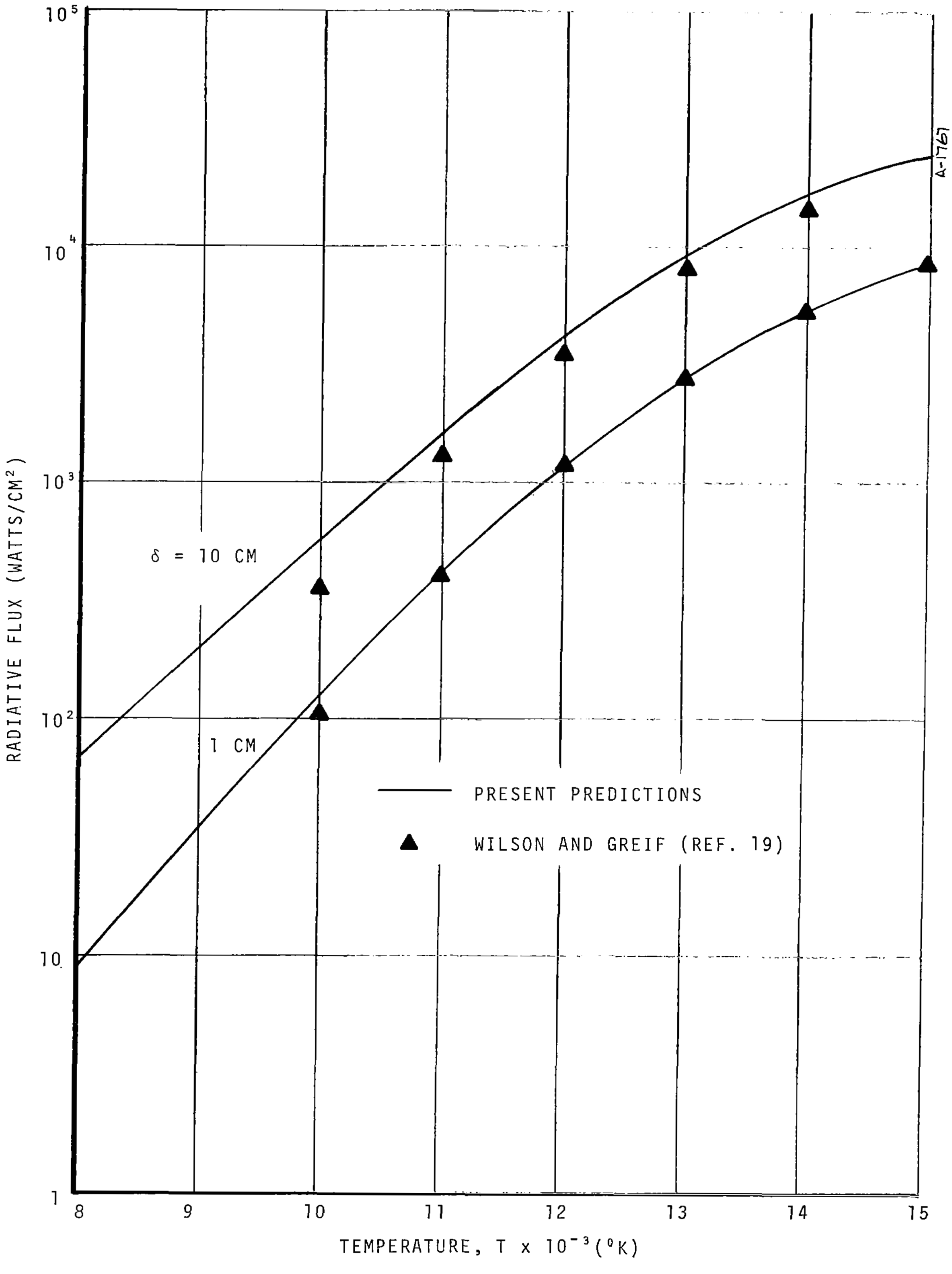

Figure 15. Flux Emitted from a Uniform Air Slab, P = 1 atm

coefficients, rather than the numerical data presented in Reference 11. While the agreement between the two is generally very good (see Fig. 2), an error exists in the 1.5 - 4 ev range which is sufficient to cause the differences observed.

A comparison with the theoretical predictions of air by Biberman et al. (Refs. 17 and 28) is given in Figure 16. The differences between their property data and that used in the present study are not large for the line radiation, both f-numbers and line widths being in good agreement. Further, the properties used for the molecular species contributions are from the same source (Ref. 28). The differences are slightly more appreciable in the case of the continuum radiation properties. They use Equation (41) and include a contribution from the N^- ion. The addition of the N^- continuum in the 1.5 ev to 4 ev spectral region more than compensates (usually) for the differences between Equation (41) and the data given in Reference 11. Thus, the fluxes Biberman et.al. (Refs.17 and 28) predicts are consistently higher than those predicted in the present study. However, reference to Figure 16 indicates that the differences are not large.

A comparison with the theoretical predictions of Hunt and Sibulkin (Ref. 9) for pure nitrogen is given in Figure 17. They obtained their molecular species contributions from Allen (Ref. 57), their continuum radiation from the tabulations of Sherman and Kulander (Ref. 58), their f-numbers from Kelly (Ref. 59) and their half widths from Griem (Ref. 18). The tabulations of Sherman and Kulander (Ref. 58) are somewhat higher than those used in the present study (Ref. 11). None of the data obtained from the other sources is significantly different from that used in the present study. Hunt and Sibulkin do handle the transport slightly differently in that J-splitting is considered and quasi-static line profiles are used for some of the higher lines. However, reference to Figure 17 indicates that these differences are not significant as good agreement exists between the two sets of predictions.

A comparison with the theoretical predictions of Lasher et.al. (Ref. 12) for hydrogen is given in Figure 18. The classical formulas for f-numbers and continuum absorption coefficients were used in both studies. However, Lasher et.al. (Ref.12)) utilize somewhat different line shapes (Eqs. (46)-(48), only), and they employ the equivalent width approximation. In addition, Lasher et.al. (Ref.12) are concerned only with the atomic contributions and do not include contributions from molecular or ionized species. As shown in Figure 18, their model is not applicable at ten atmospheres for the lower temperatures. However, the two sets of predictions are in good agreement at the lower pressures.

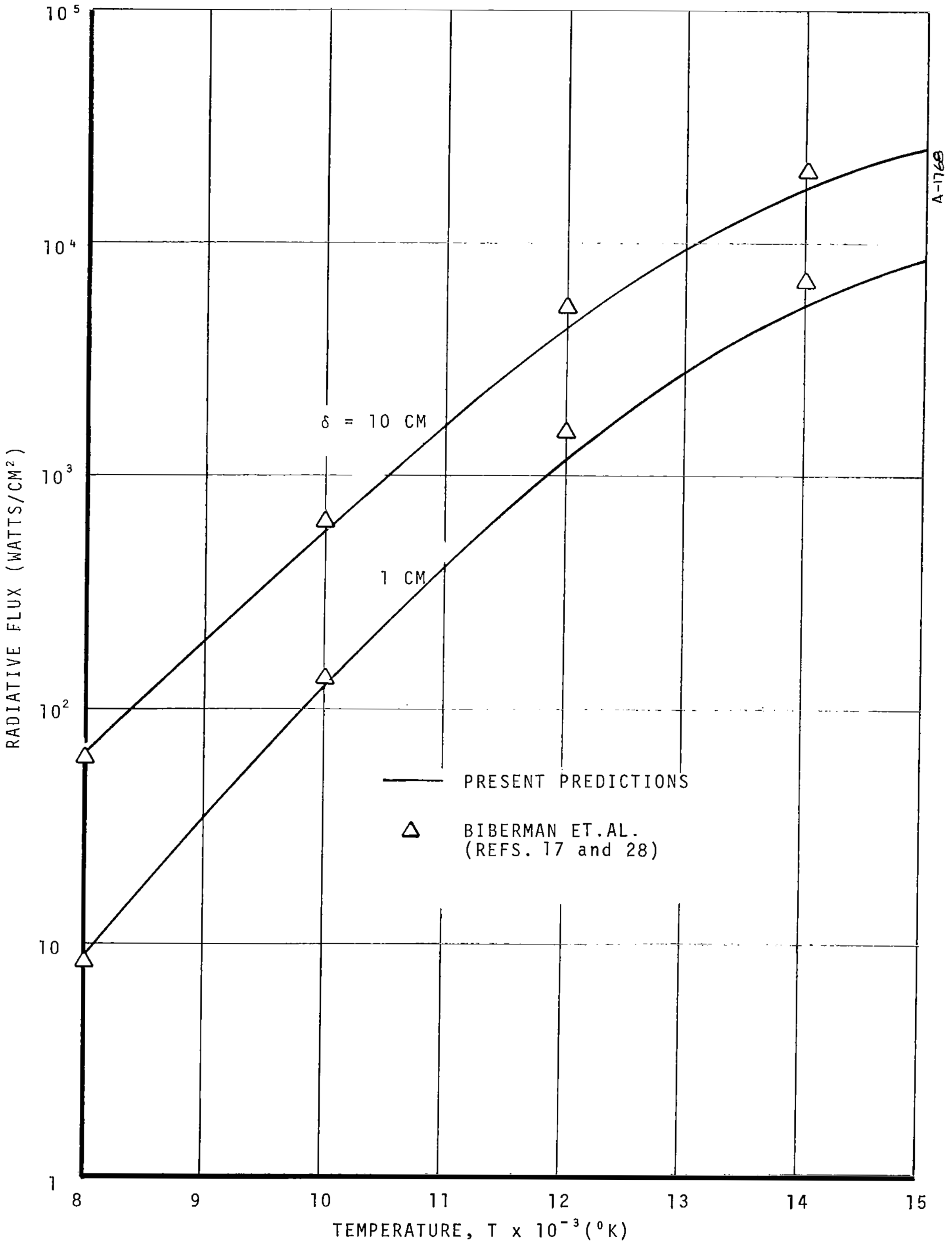

Figure 16. Flux Emitted from a Uniform Air Slab, P = 1 atm

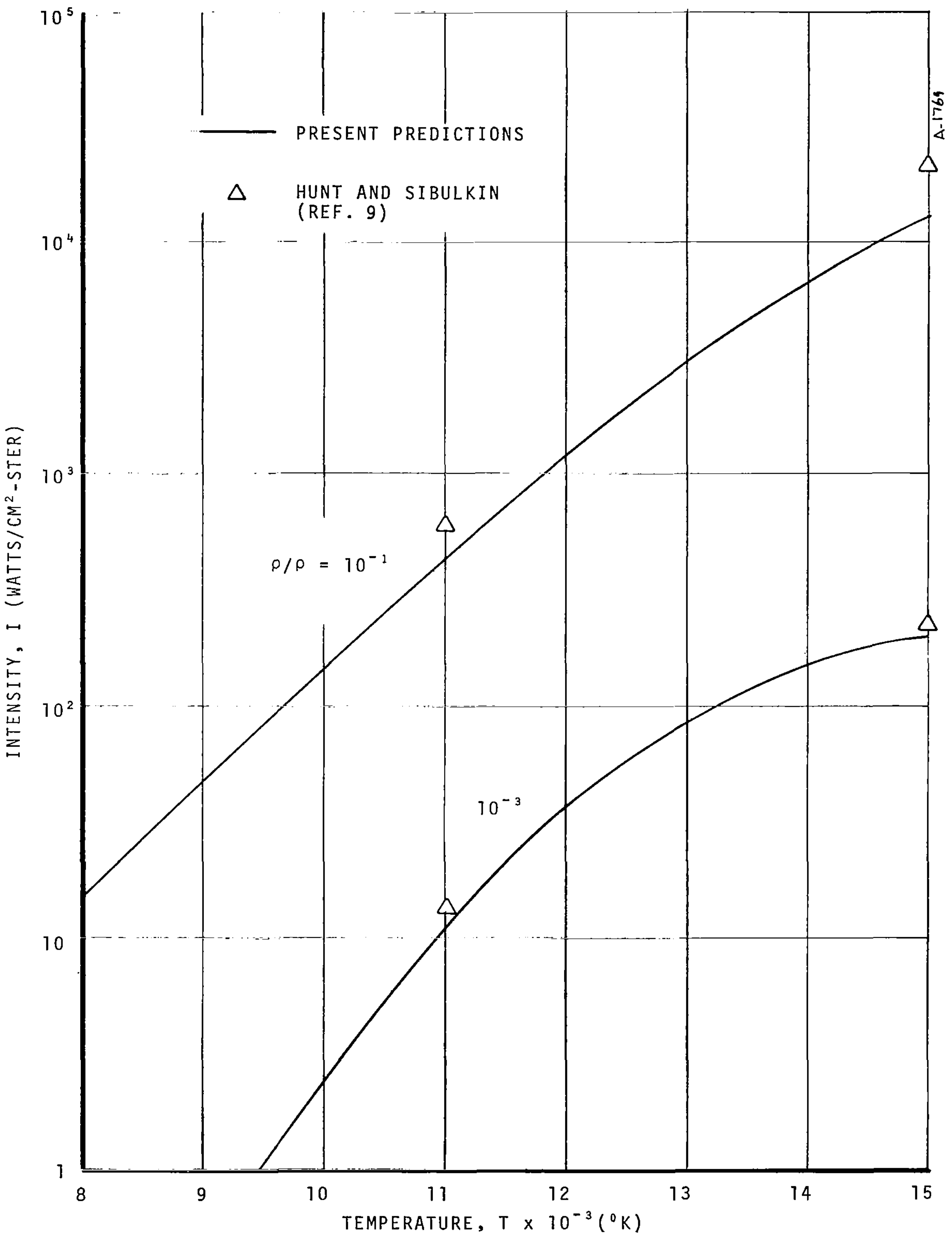

Figure 17. Intensity Emitted from a Uniform Nitrogen Slab, δ = 1 cm

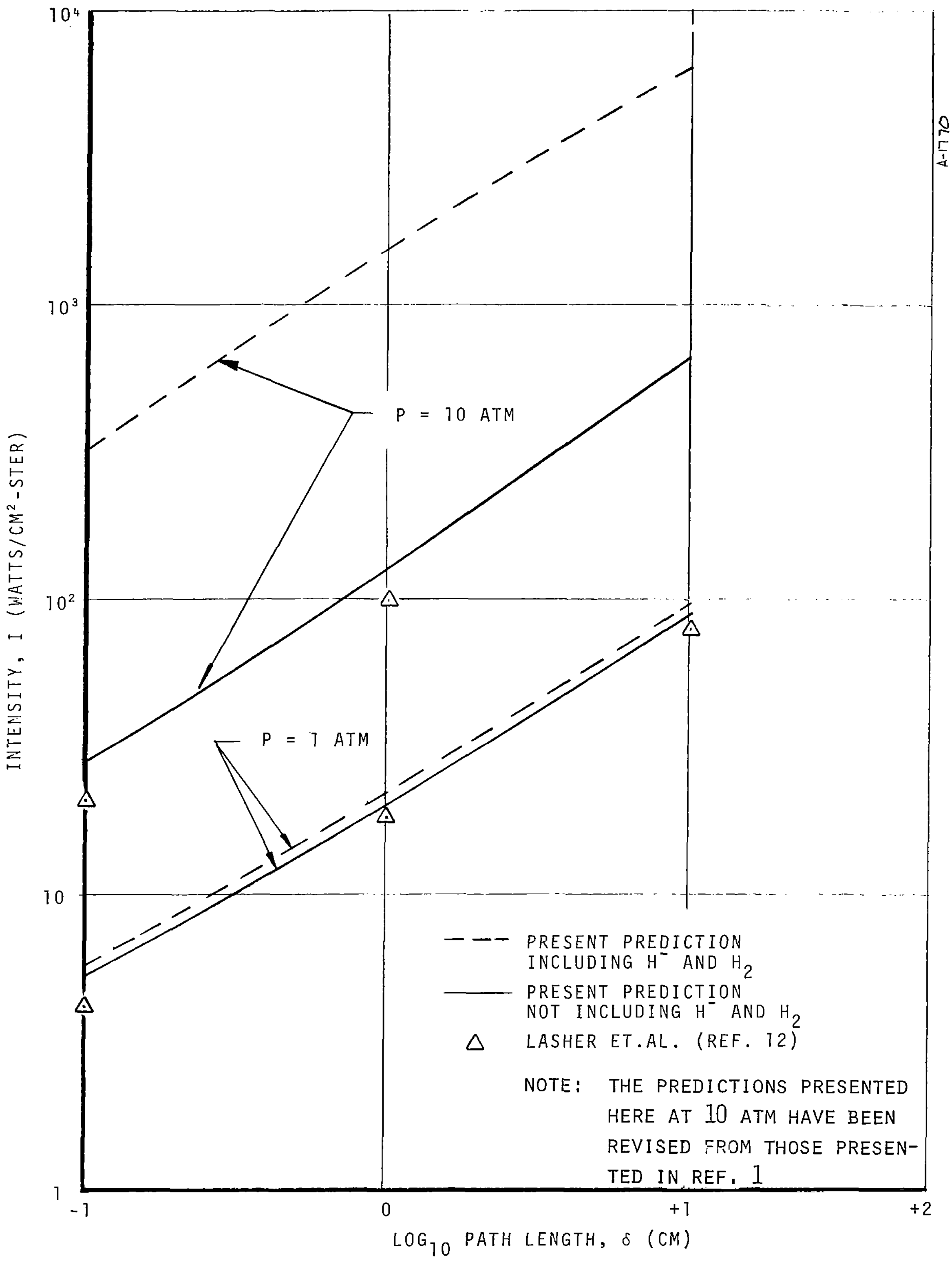

Figure 18. Intensity Emitted from a Uniform Hydrogen Slab, T = 10,000°K

5.3 COMPARISONS WITH MEASURED DATA

Predictions of the emission coefficients of shock heated air are given in Figures 19, 20, and 21 and compared with the measurements of Nerem (Ref. 60) and Gruszczynski and Warren (Ref. 61). The predictions are in excellent agreement with the data of Nerem (Ref. 60), but they are slightly lower than the data of Gruszczynski and Warren (Ref. 61). The basic techniques used in the two experimental studies are very similar, and the same general range of conditions were covered. It is unfortunate that the two sets of results are not in better agreement with each other. Nevertheless, the general agreement between prediction and experiment is felt to be encouraging.

The predicted intensities of air behind a reflected shock wave are given in Figures 22 and 23 and compared with the measurements of Wood et al. (Ref. 62). The predictions are in excellent agreement with the measurements for incident shock velocities less than 7.5 mm/μ sec. and are above the measurements at higher velocities. Golobic and Nerem (Ref. 63) have analyzed a reflected shock experiment similar to that performed by Wood et al. (Ref. 62) and have concluded that the radiation losses significantly cool the gases for incident shock velocities above 7.5 mm/μ sec. They present calculated intensities for the low frequency spectrum ($\lambda > 1{,}700$ Å) showing the effect of the losses. Obtaining their predicted ratios of intensities with radiation losses to those without losses (as a function of incident shock velocity) and using them to (approximately) correct the prediction given in Figure 22 yields the dashed curve and a dramatically improved comparison between prediction and measurement. Such an effect would obviously affect the total intensities also. Clearly, this was a rough estimate but it was encouraging in that the present predictions are not necessarily inconsistent with the measurements of Wood et al. (Ref. 62).

This concludes the series of comparisons with the work of other investigators. It is felt that the model has been proven to be a valid one. Subsequent numerical work will be used to illustrate interesting applications.

5.4 APPLICATION TO UNIFORM SLABS

Theoretical predictions for uniform slabs are given in Figures 24 and 25. They show the variation of the fluxes emitted from uniform slabs of air. The ranges of temperature, pressure and path lengths selected are typical of those which might be encountered in the stagnation region of a vehicle reentering from a lunar or planetary mission.

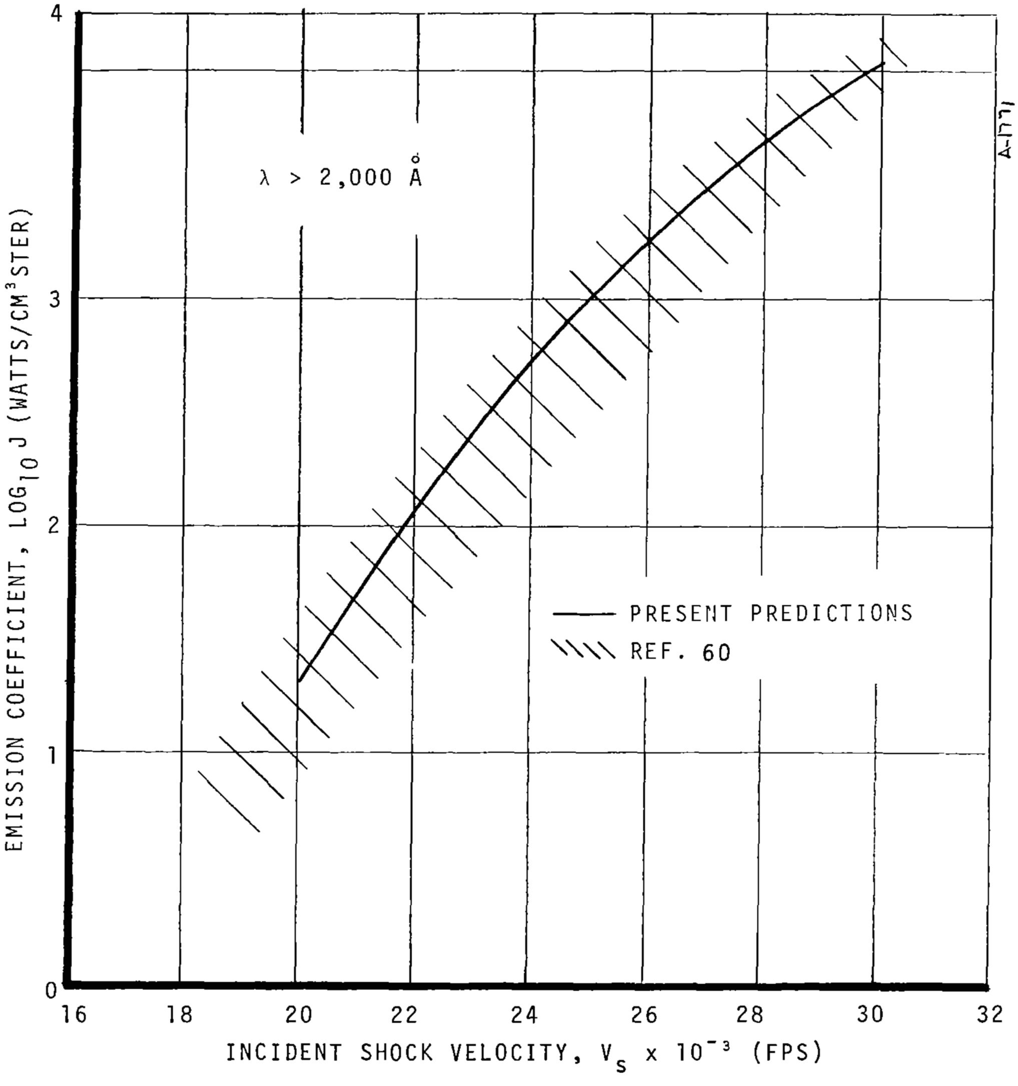

Figure 19. Comparison with the Shock Tube Data of Nerem (Ref. 60), P_1 = 1 mm Hg

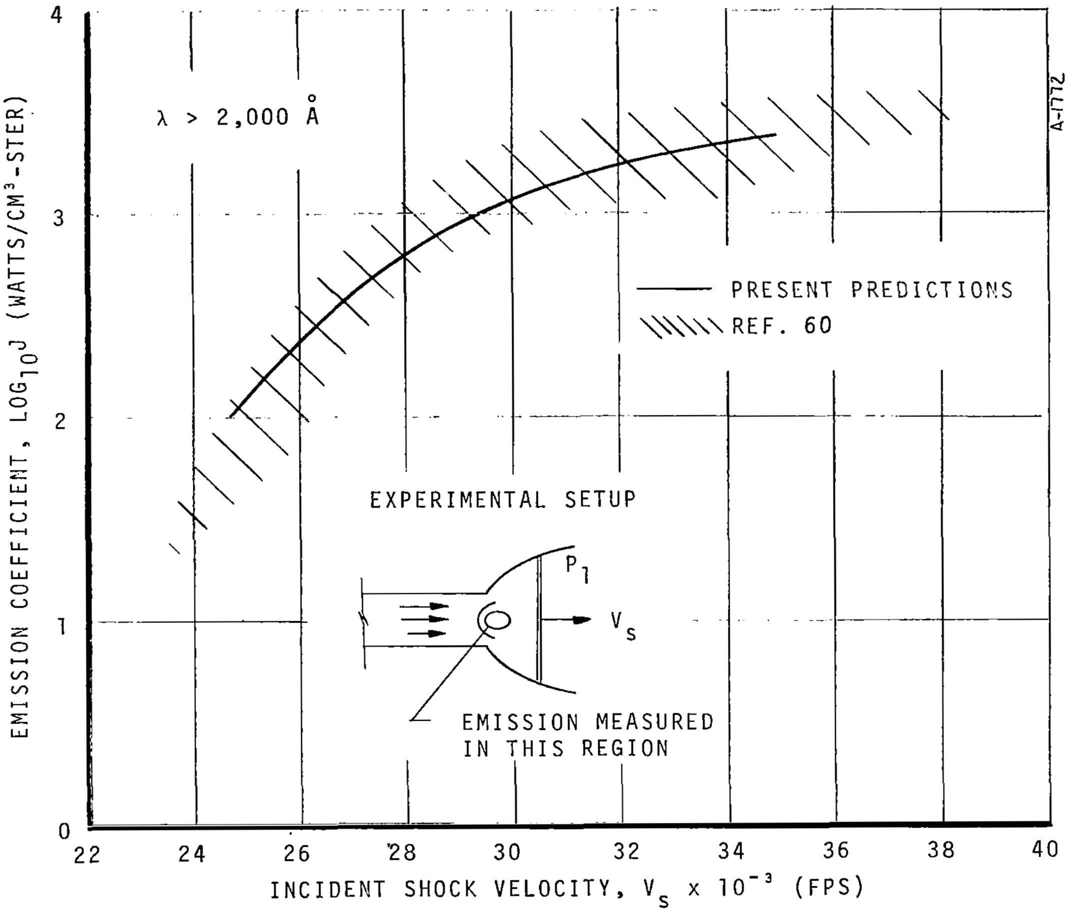

Figure 20. Comparison with the Shock Tube Data of Nerem (Ref. 60), P_1 = 2 mm Hg

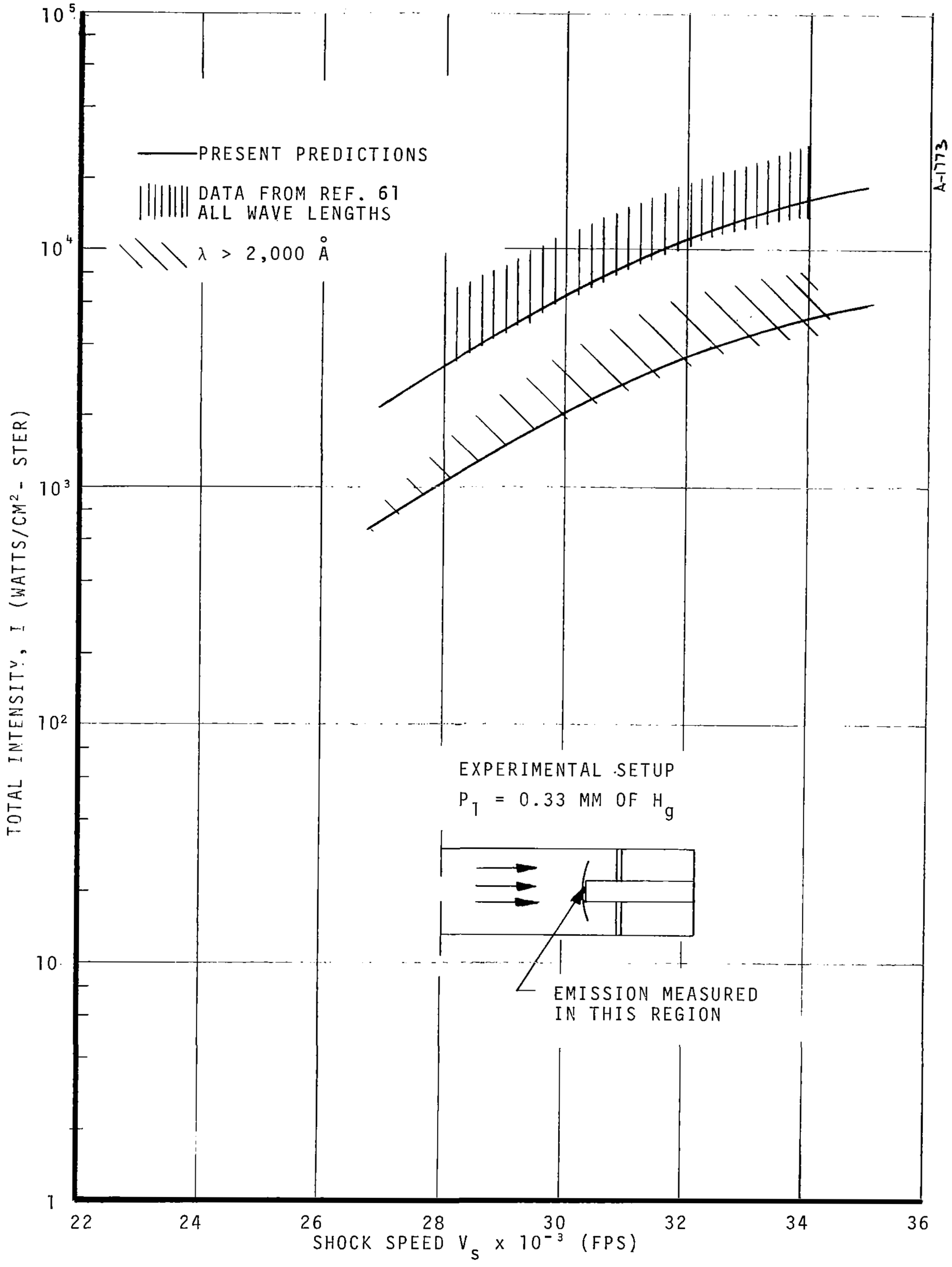

Figure 21. Comparison with Shock Tube Data of Gruszynski and Warren (Ref. 61)

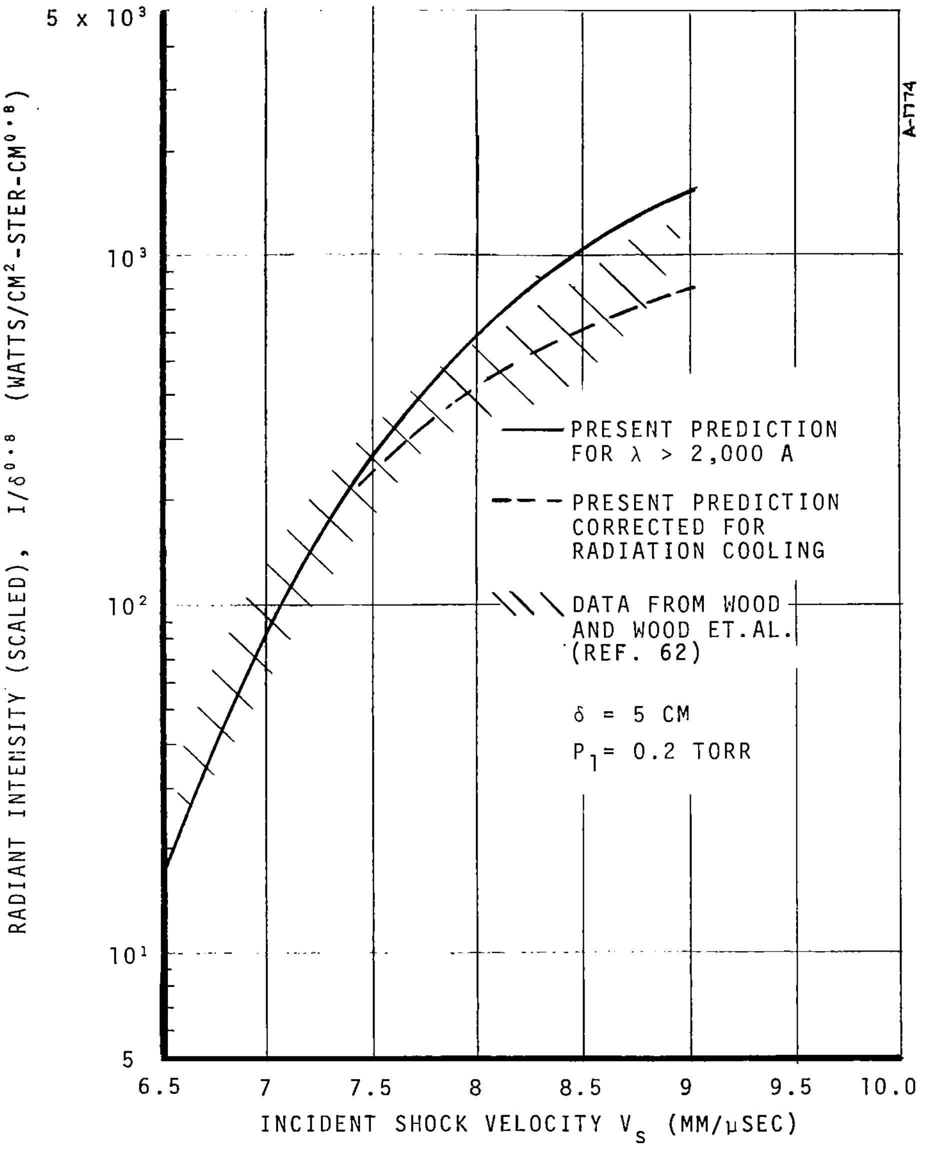

Figure 22. Comparison with Shock Tube Data of Wood (Ref. 62)

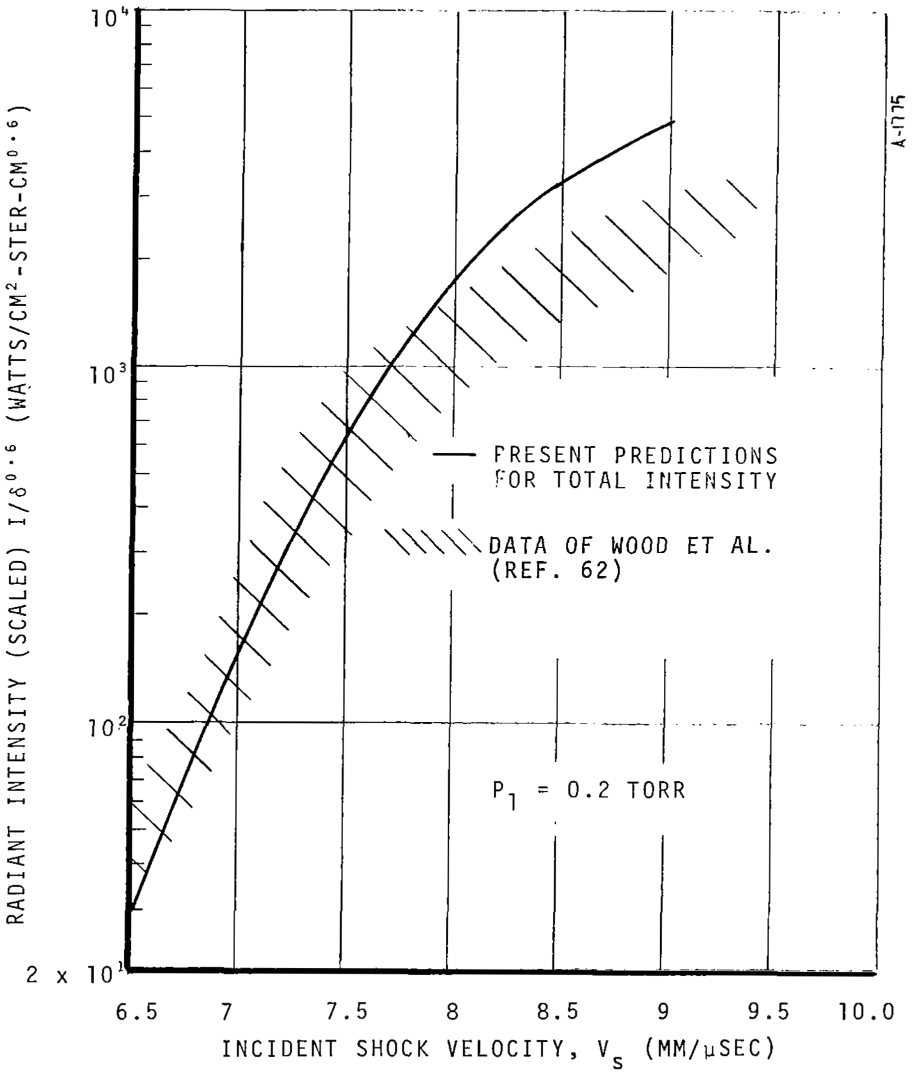

Figure 23. Comparison with Total Intensity Measurements of Wood (Ref. 62)

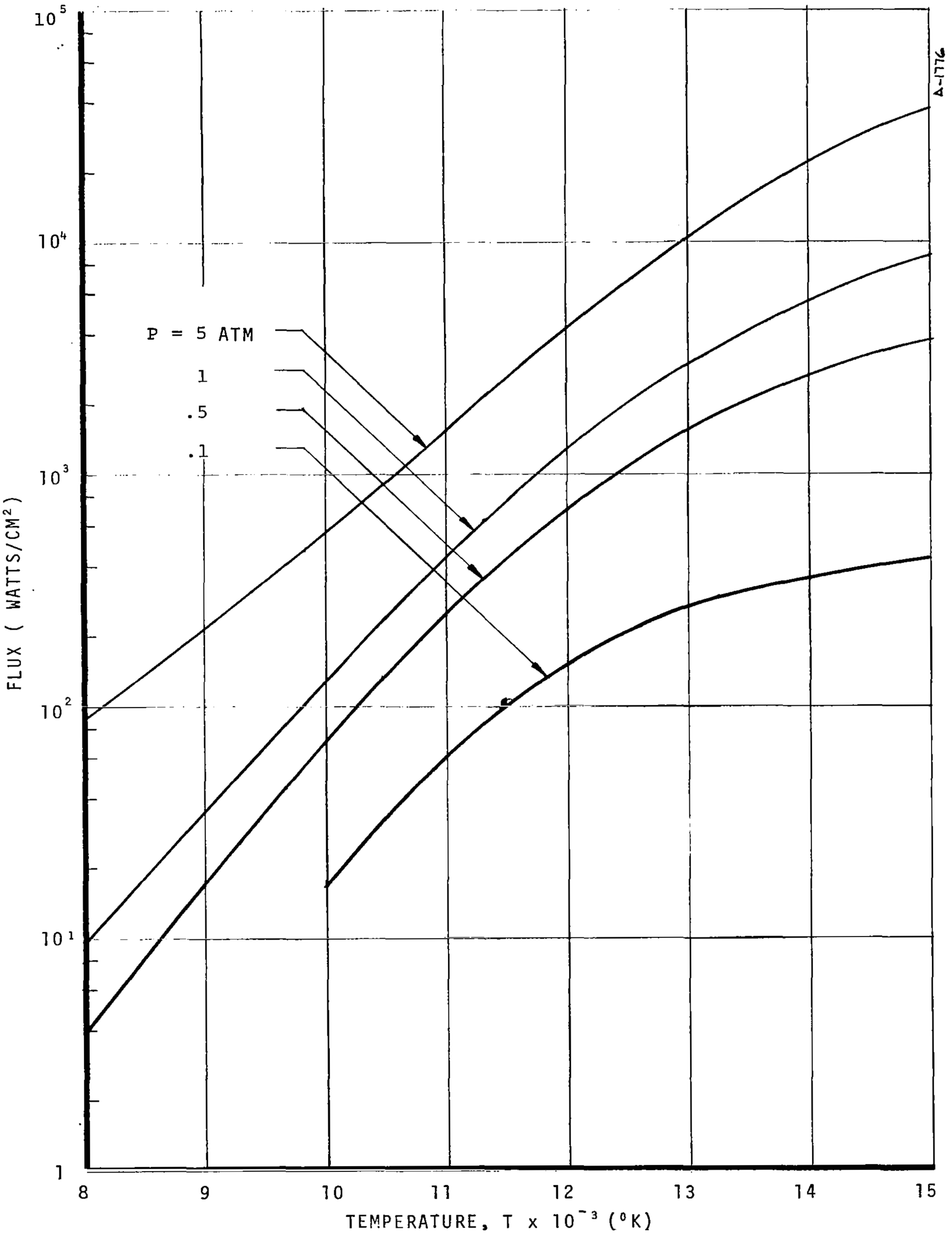

Figure 24. Variation of Flux from a Uniform Air Slab, δ = 1 cm

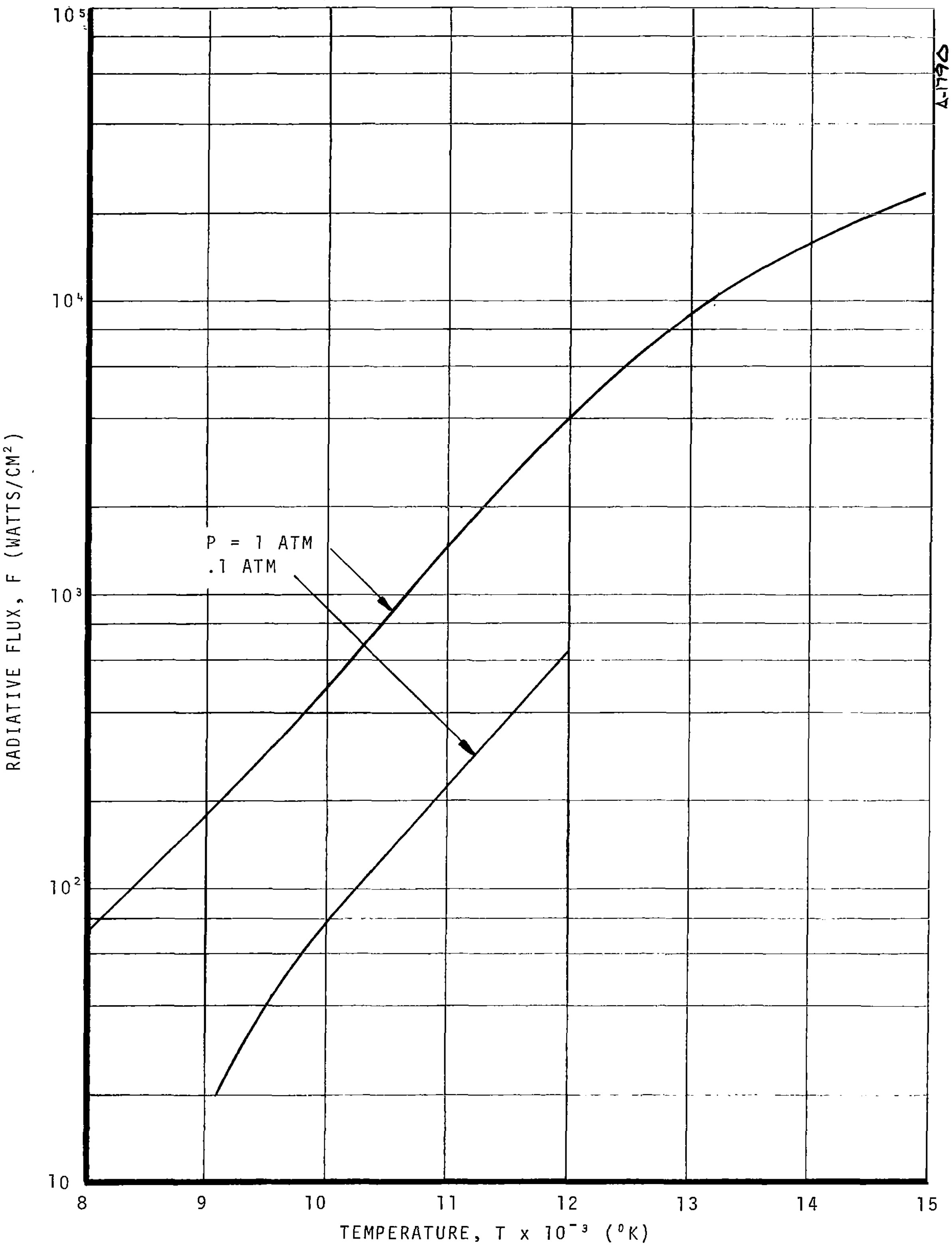

Figure 25. Variation of Flux from a Uniform Air Slab, δ = 10 cm

5.5 APPLICATION TO NONUNIFORM SLABS

To further illustrate applications of the method, a slab with nonuniform properties was selected and its distributions of flux in space and frequency obtained. The variations of the thermodynamic state properties across the slab are given in Figure 26 where the overall length of the slab (y_δ) is 11.4 cm. This variation is typical of that which might be found in the stagnation region of a vehicle reentering from a lunar mission. Carbon and hydrogen gases were included as they are usually present due to mass injection from the surface of the vehicle.

The spatial distribution of the radiation species is given in Figure 27. The molecules reside in a narrow region immediately adjacent to the wall ($y/y_\delta < 0.01$). In this case the region was so narrow that it had essentially no interaction with the radiation field. A mixing region exists further out where transition from mainly atomic to mainly molecular species occurs ($0.01 < y/y_\delta < 0.1$). The species in this region tend to emit in the visible and absorb in the ultraviolet. Note that atomic carbon and hydrogen are present in significant quantities. The exterior field ($y/y_\delta > 0.1$) consists of pure air species. In this case, the atomic species dominate with the N contributions being of particular importance.

The spectral distribution of the positive continuum fluxes (directed toward the wall) are shown in Figure 28, both at the wall and at the edge of the boundary layer (which is set arbitrarily at $y/y_\delta = 0.211$). The peaks in the wall flux at $h\nu = 1$ ev and 3.3 ev are primarily due to emission from the red and violet CN bands in the boundary layer. There is also a peak in the boundary flux at $h\nu = 3.3$ ev, but this must be attributed to $N_2^+(1-)$ (a trace species) emission from the exterior flow region. The ultraviolet contributions to the boundary flux above 10.8 ev are due to N emission from its photoionization edges with the flux levels beyond 12 ev being nearly black body. Note that the wall flux has undergone severe attenuation in the region $h\nu > 11.5$ ev. This is due to absorption by the photoionization edges of the carbon atoms in the mixing region. Typically, large fractions of the incident ultraviolet continuum will be absorbed in the boundary layer.

The spectral distribution of the wall flux is presented again in Figure 29, but here the contributions from the line groups are also included.* The

---

*For this application, the RAD/EQUIL program calculated line fluxes integrated over the line groups (as discussed in Section 3.2.2), rather than spectral fluxes. Consequently, the redistribution over the spectrum shown in Figure 29 has been smoothed and employs some artistic license.

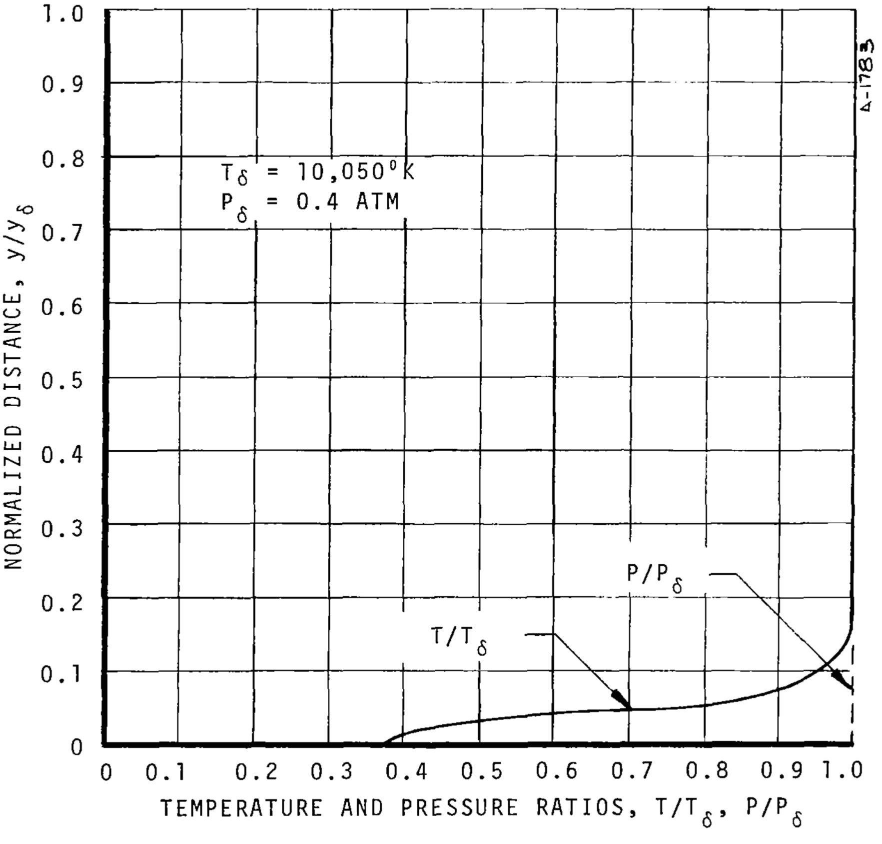

Figure 26. Thermodynamic State Variation

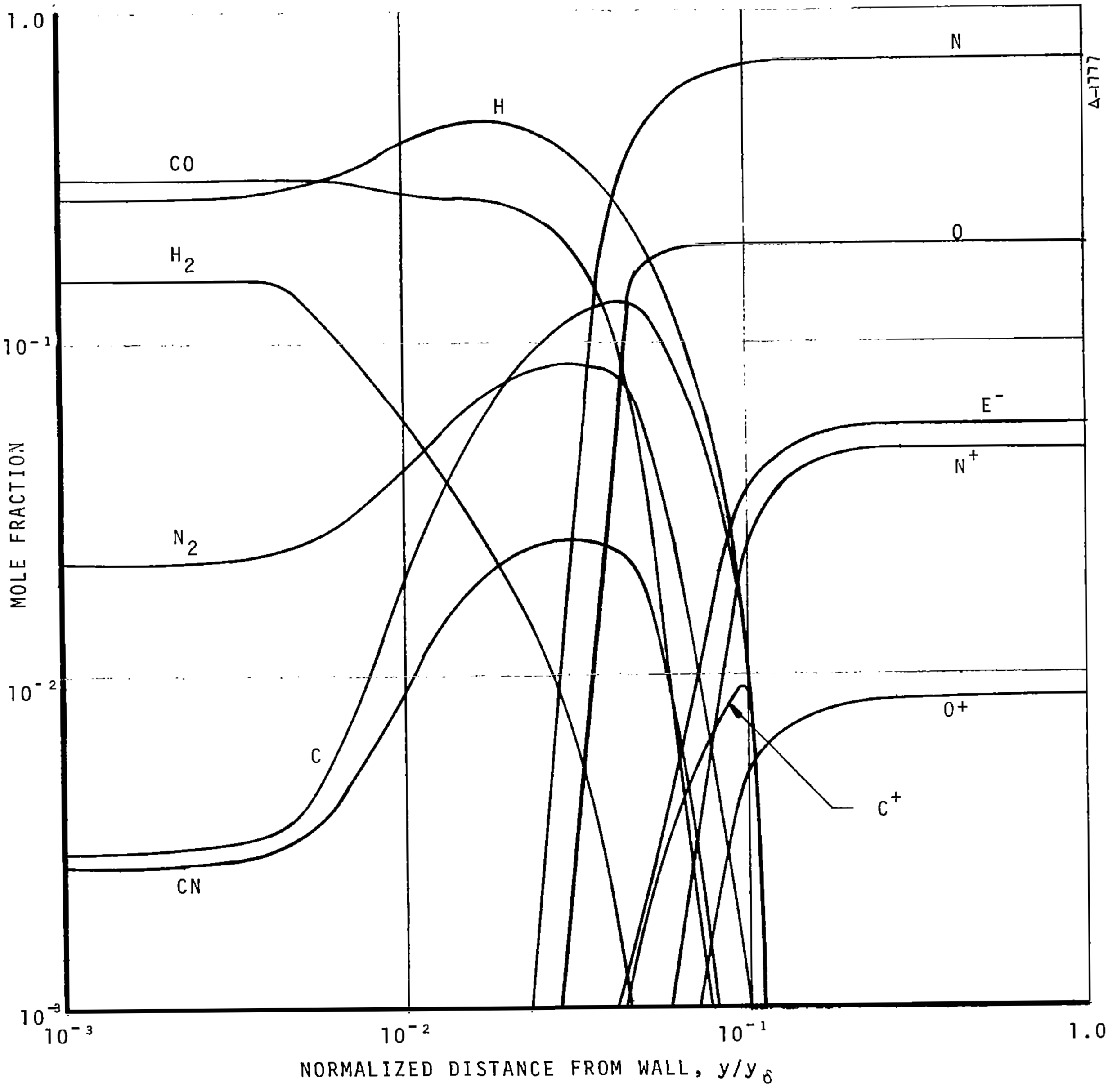

Figure 27. Spatial Distribution of Radiating Species

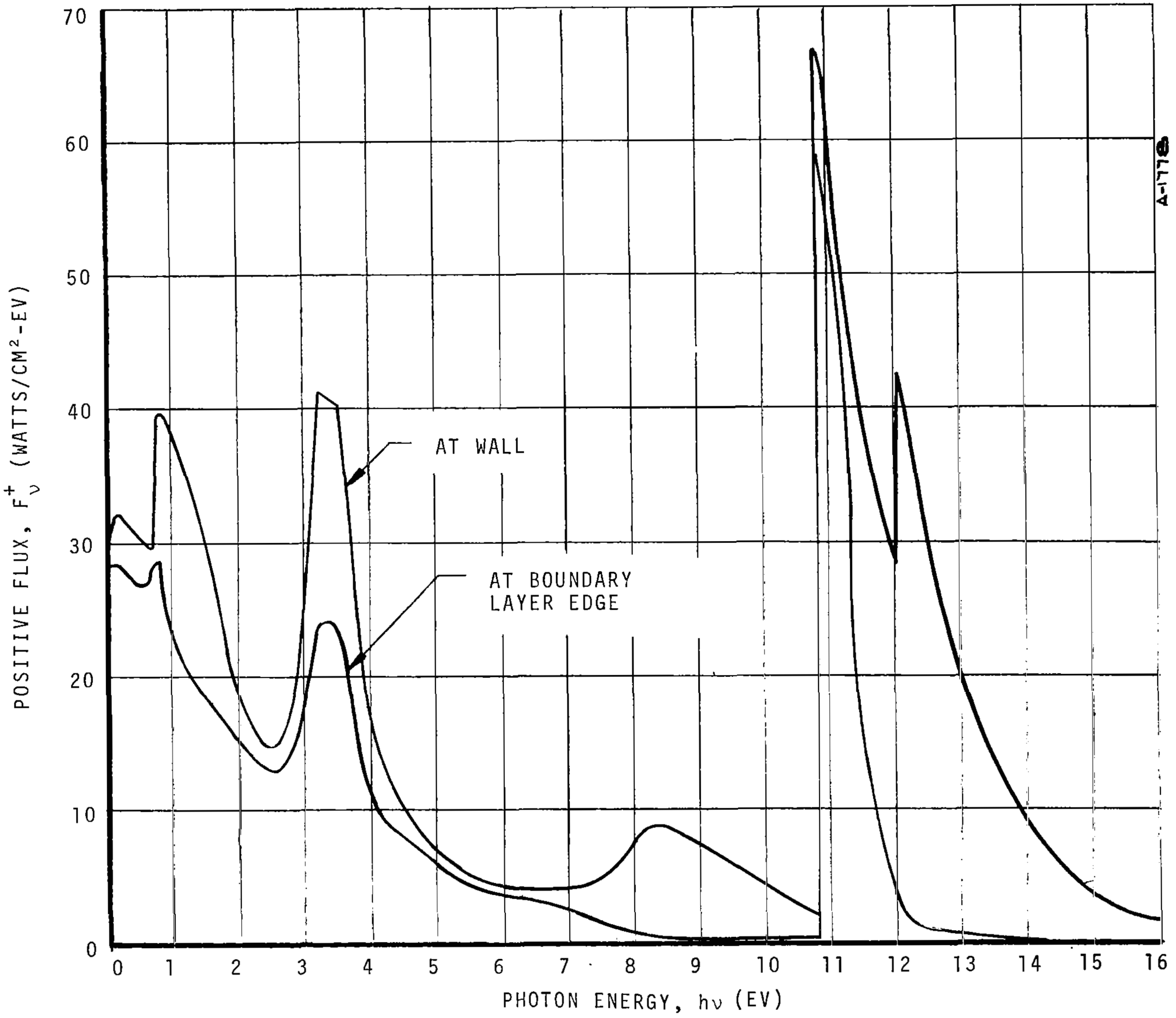

Figure 28. Spectral Distribution of Continuum Fluxes

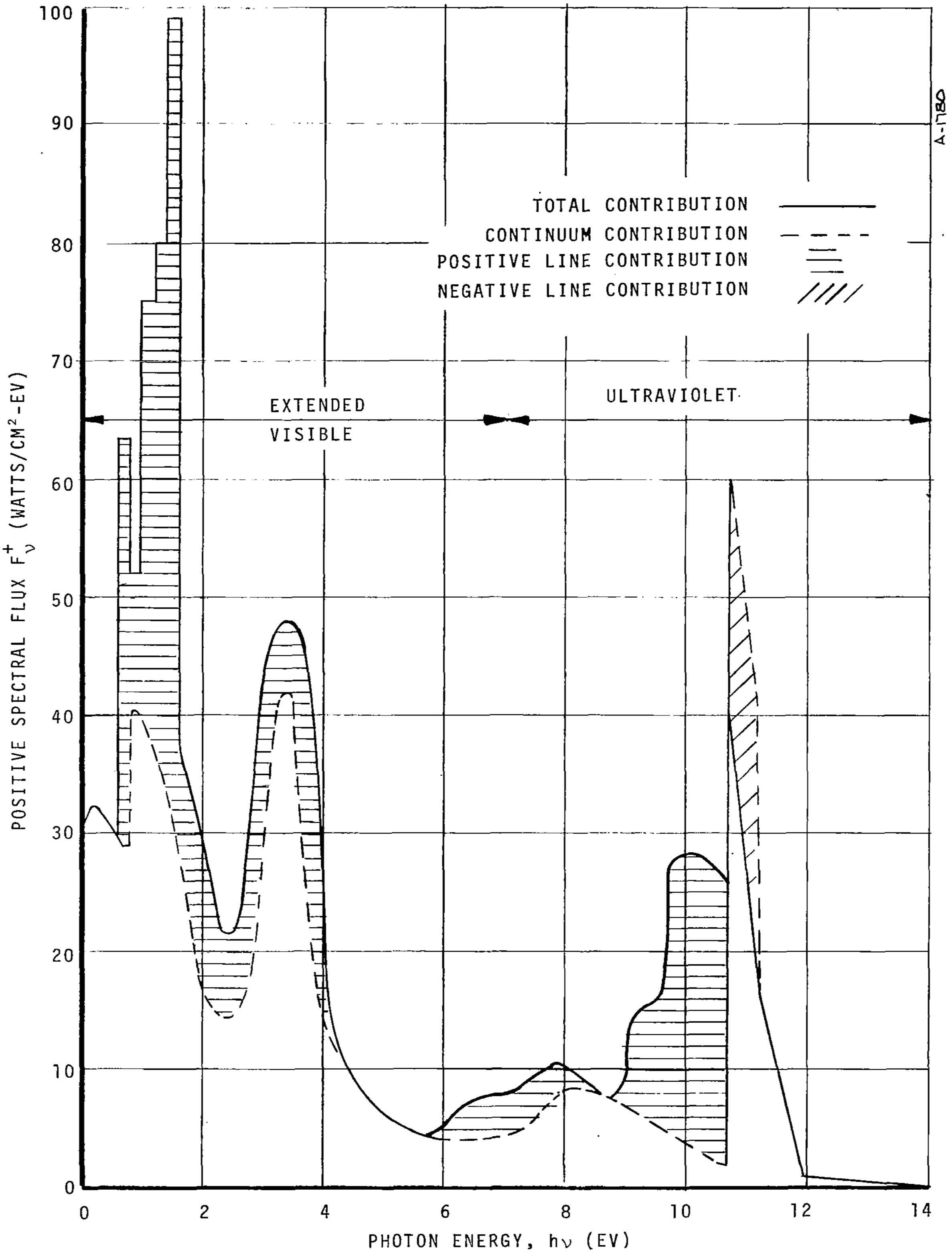

Figure 29. Spectral Variation of Positive Flux at Wall

line contribution is extremely important (probably dominant) in the visible region. Here the line fluxes are substantially higher than those of the background continuum, viz. bright lines. In the ultraviolet region the lines contribute a modest addition to the flux in the 9-10.8 ev range. However, in the 10.8-11.5 ev range the line fluxes are less than the background continuum fluxes, viz. dark lines, and the total flux to the wall is significantly less than it would have been if line contributions had not been included. This is also typical as the ultraviolet lines can be strongly absorbed in nonisothermal regions.

The energy exchange mechanism between the boundary layer and the exterior flow is illustrated further in Figures 30 and 31. The spatial variation of the transmitted fraction of the positively directed total flux and the relative fractions of its constituents are shown in Figure 30. Thus, the positive flux undergoes a steady attenuation from $\eta \approx 6$ to $\eta \approx 0.75$ with the ultraviolet continuum accounting for the bulk of the loss. For $\eta < 0.75$ the loss rate increases noticeably due to line attenuation. The effect is further illustrated in Figure 31 where the spatial variation of the net flux is shown. The region $6 < \eta < 0.7$ shows that the entering flux is always less than the departing flux causing radiative cooling. Nearer the wall ($\eta < 0.7$) the effect reverses causing radiative heating. Thus, the following qualitative effects are present: (a) the gases near the wall are heated, (b) the gases in the outer regions of the boundary layer are cooled, (c) the emission from the ablated species in the boundary layer is not sufficient to offset the losses from the boundary flux by absorption and (d) the boundary flux is attenuated significantly (in this case by 25 percent) before it reaches the wall.

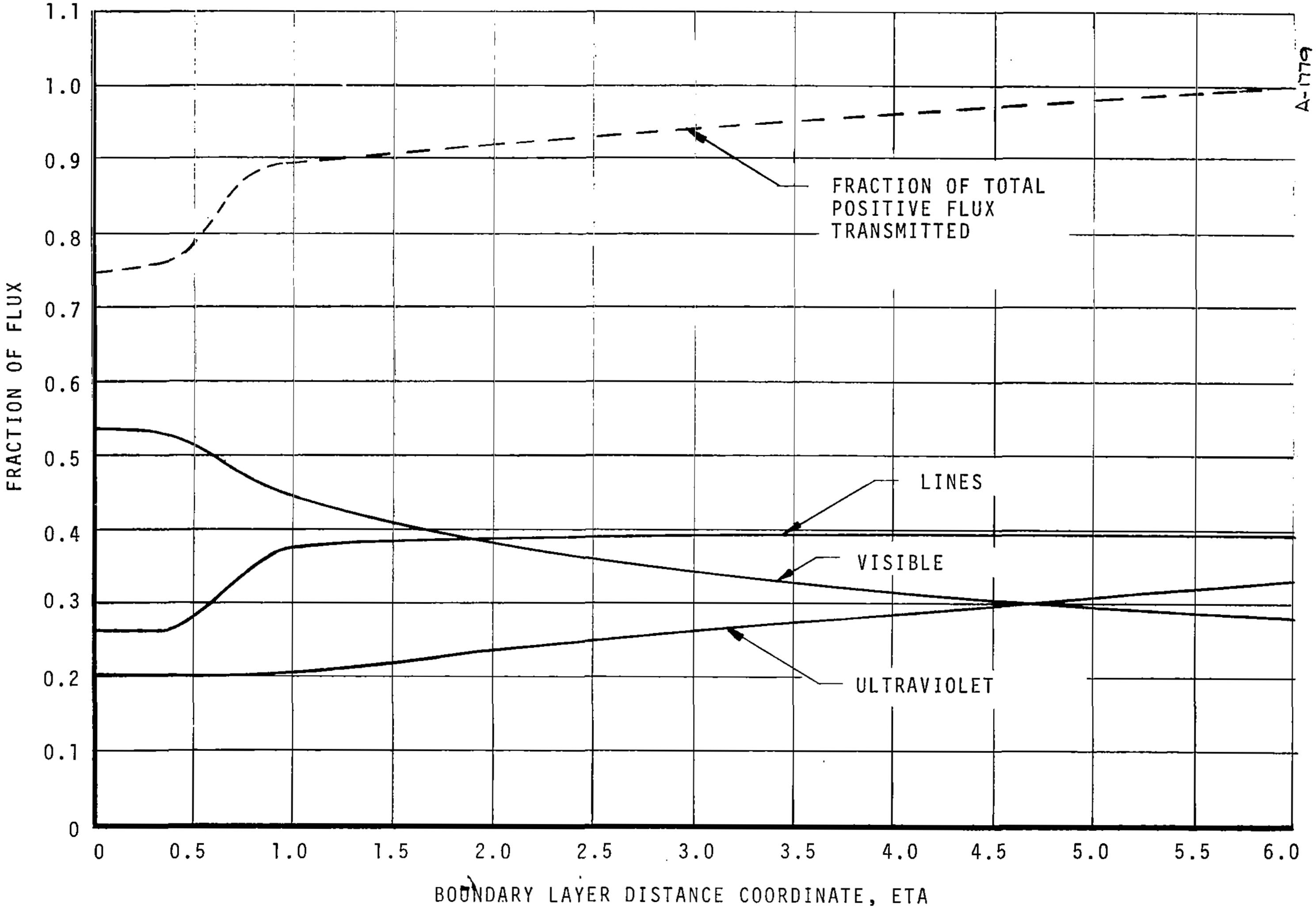

Figure 30. Positive Flux Variation

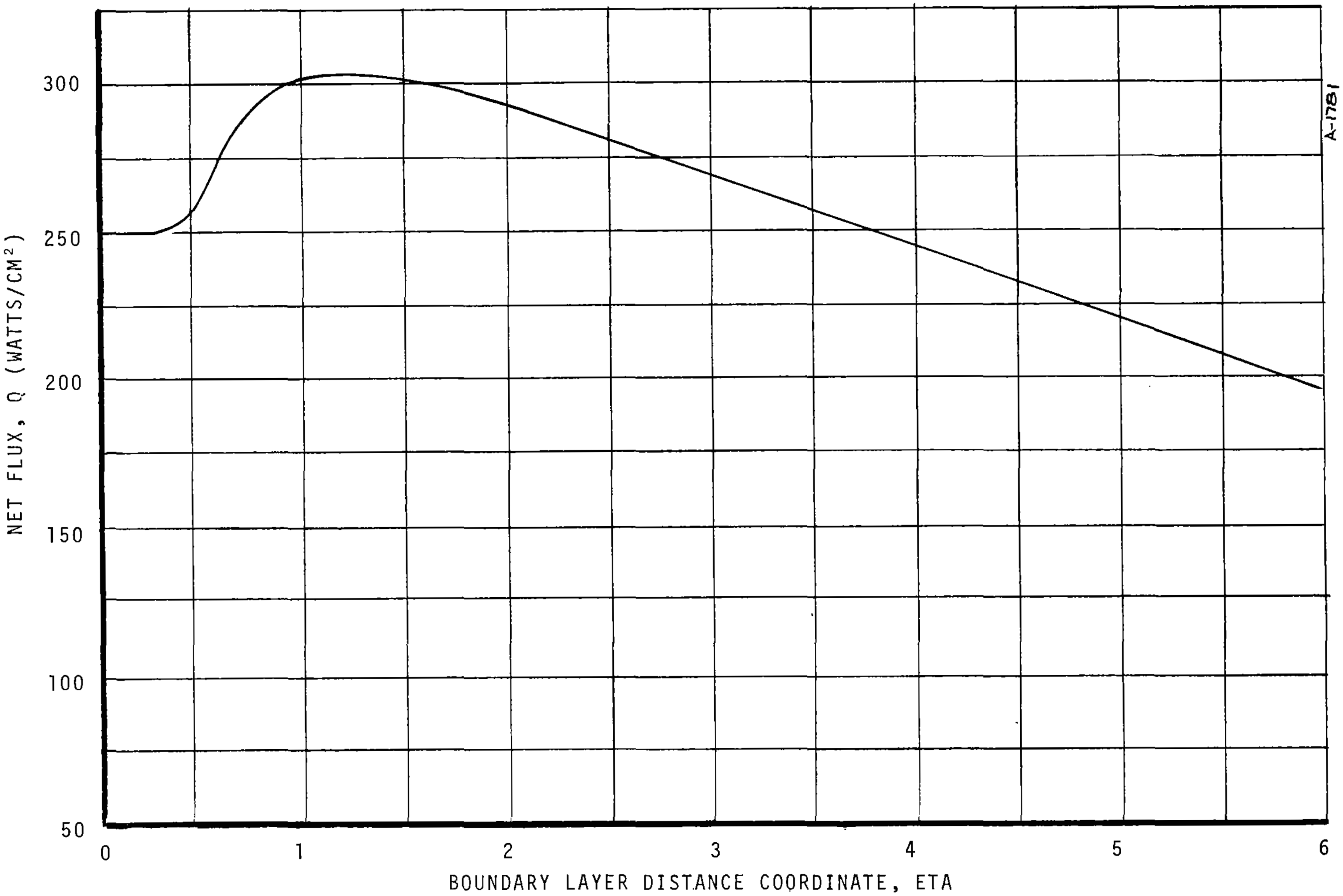

Figure 31. Net Flux (Positive When Directed Toward the Wall)

SECTION 6

CONCLUDING REMARKS

A prediction method has been described which can be used to obtain fluxes or intensities at any specified point within a plane-parallel slab (for the flux calculation) or at any point on a ray (for the intensity calculation). While the method was developed for the study of radiation heating phenomena within the mass injected boundary layer environment, it is not limited to such studies. Indeed, its primary virtue is its versatility. The only approximation which is an integral part the method is the bandless model for the molecular bands. Any of the other aspects of the properties model can easily be made to include more (or less) detail, allowing important trade-offs to be made between accuracy and computational effort.

The comparisons presented in Sections 5.1 to 5.3 showed that the present predictions are in generally good agreement with predictions from other studies. Comparison with available experiments yielded no additional information as the inconsistencies between the different sets of experimental data are greater than are those between the sets of predictions.

SECTION 7

REFERENCES

1. Nicolet, W.E.: A Nongrey Radiation Transport Model Suitable for Use in Ablation-Product Contaminated Boundary Layers. NASA CR-92473, Aerotherm Corporation, Mountain View, California, October 15, 1968.

2. Kendall, R.M.: A General Approach to the Thermochemical Solution of Mixed Equilibrium-Nonequilibrium, Homogeneous or Heterogeneous Systems. NASA CR-1064, Aerotherm Corporation, Mountain View, California, June 1968.

3. Deblaye, C. and Bartlett, E.P.: An Evaluation of Thermodynamic and Transport Properties for Use in the BLIMP Nonsimilar Multicomponent Boundary-Layer Program. Report 69-53, Aerotherm Corporation, Mountain View, California, July 1969.

4. Browne, H.N., Williams, M.N., and Cruise, D.R.: The Theoretical Computation of Equilibrium Compositions, Thermodynamic Properties, and Performance Characteristics of Propellant Systems. NOTS TP 2434, NAVWEPS Report 7043, (ASTIA AD 246591), June 1960.

5. Anon.: JANAF Thermochemical Tables, The Dow Company, Midland, Michigan, including revisions through August 1967.

6. Hochstim, A.R.: Equilibrium Compositions, Thermodynamic and Normal Shock Properties of Air With Additives. General Dynamics, Convair Report ZPH-122, 1961.

7. Gilmore, F.R.: Thermal Radiative Phenomena, Vol. 1, The Equilibrium Thermodynamic Properties of Air. Lockheed Report 3-27-67-1, Vol. I, May 1967.

8. Gilmore, F.R.: Equilibrium Properties and Thermodynamic Properties of Air to 24,000 K. Rand Research Memorandum RM 1543, August 1955, ASTIA AD 84052, also RM 3748-PR, 1963.

9. Hunt, B.L. and Sibulkin, M.: Radiation Transfer in a Gas of Uniform Properties in Local Thermodynamic Equilibrium, Part I, Part II, and Part III. Brown Univ. Report No. NONR-562(35)/18, December 1966.

10. Karzas, W.J. and Latter, R.: Electron Radiative Transitions in a Coulomb Field. Astrophys. J.Supplement, 6, 167, 1961.

11. Wilson, K.H. and Nicolet, W.E.: Spectral Absorption Coefficients of Carbon, Nitrogen and Oxygen Atoms. JQSRT, 7, 891, 1967.

12. Lasher, L.E., Wilson, K.H. and Greif, R.: Radiation from an Isothermal Hydrogen Plasma at Temperatures Up to $40,000^{\circ}K$. Lockheed MSC Report No. 6-76-66-17, Revised, July 1967.

13. Burgess, A. and Seaton, M.J.: A General Formula for the Calculation of Atomic Photo-Ionization Cross Sections. Mon. Not. R. Astr. Soc., 120, 121, 1961.

14. Armstrong, B.H., Johnston, R.R., and Kelly, P.S.: Opacity of High Temperature Air. Lockheed Missiles & Space Co., Report No. 8-94-64-2 (also Air Force Weapons Lab. Report AFWL-tr 65-17), 1964.

15. Biberman, L.M. and Norman, G.E.: Recombination Radiation and Bremsstrahlung of a Plasma. JQSRT, 3, 221, 1963.

16. Hahne, G.E.: The Vacuum Ultraviolet Radiation from N^+ and O^+ Electron Recombination in High Temperature Air. NASA TND-2794, June 1965.

17. Biberman, L.M., Vorob'ev, V.S., Norman, G.E., and Iakubov, I.T.: Radiation Heating in Hypersonic Flow. Kosmich, Issled., Vol. 2, No. 3, 1964, pp. 441-454.

18. Griem, H.R.: Plama Spectroscopy. McGraw-Hill Book Co., New York, 1964.

19. Wilson, K.H. and Greif, R.: Radiation Transport in Atomic Plasmas. Lockheed MSC Report No. 6-77-67-31, November 1967.

20. Page, W.A., Compton, D.L., Borucki, W.J., Ciffone, D.L., and Cooper, D.M.: Radiative Transport in Inviscid Nonadiabatic Stagnation-Region Shock Layers. AIAA Paper No. 68-784, June 1968.

21. Condon, E.U. and Shortley, G.H.: The Theory of Atomic Spectra. Cambridge University Press, London, 1935.

22. Griem, H.R., Kolb, A.C., and Shen, R.V.: Start Broadening of Hydrogen Lines in Plasma. NRL Report 5455, 1960.

23. Griem, H.R.: Stark Broadening of Higher Hydrogen and Hydrogenlike Lines by Electrons and Ions.: Astrophys. J., 132, 883, 1960.

24. Kepple, P.C.: Improved Stark Profile Calculations for the First Four Members of the Hydrogen Lyman and Balmer Series. Report No. 831, Univ. of Maryland, College Park, Maryland, 1968 Also, Phys.Rev.,173, 317, 1968.

25. Armstrong, B.H.: Apparent Positions of Photoelectric Edges and the Merging of Spectrum Lines. JQSRT, 4, 207, 1964.

26. Vorobyov, V.S. and Norman, G.E.: Energy Radiated in Spectral Lines by an Equilibrium Plama, II. Optics & Spec., 14, 96, 1963.

27. Aroeste, H., and Magee, J.L.: Thermal Radiation Phenomena, Vólume 3, Tables of Radiative Properties of Air. Lockheed Report LMSC 3-27-67-1, Vol. 3, May 1967.

28. Biberman, L.M., Mnatsakanyan, A.Kh.: Optical Properties of Air in the Temperature Range from 4,000 to 10,000°K. Teplotizika Vysokikh Temperatur, 4, 148, 1966.

29. Churchill, D.R., Hagstrom, S.A. and Landshoff, R.K.M.: The Spectral Absorption Coefficient of Heated Air. JQSRT, 4, 291, 1964.

30. Lofthus, A.: The Molecular Spectrum of Nitrogen, Spectroscopic Report No. 2, Dept. of Physics, University of Oslo, Blindern, Norway, 1960.

31. Gilmore, F.S.: The Contribution of Generally-Neglected Band Systems and Continua to the Absorption Coefficient of High-Temperature Air. JQSRT, 5, 125, 1965.

32. Watanabe, K., J. Chem. Phys., 22, 1954.

33. Appleton, J.P. and Steinberg, M.: Vacuum-Ultraviolet Absorption of Shock-Heated Vibrationally Excited Nitrogen. J.Chem, Phys., 46, 1521, 1967.

34. Allen, R.A.: Radiation Graphs, Spectrally Integrated Fluxes Including Line Contributions and Self-Absorption. AVCO Research Report 230, September 1965.

35. Churchill, D.R., Armstrong, B.H. and Mueller, K.G.: Absorption Coefficient of Heated Air: A Compilation to 24,000°. Lockheed Report 4-77-65-1, 1965.

36. Arnold, J.O., Reis, V.H., and Woodward, H.T.: Studies of Shock-Layer Radiation of Bodies Entering Planetary Atmospheres. AIAA 2, 2019, 1965.

37. Woodward, H.T.: Predictions of Shock-Layer Radiation from Molecular Band Systems in Proposed Planetary Atmospheres. NASA Technical Note, NASA TN D-3850, Ames Research Center, Moffett Field, California, February 1967.

38. Main, R.P., and Bauer, E.: Opacities of Carbon-Air Mixtures at Temperatures from 3000-10,000°K. JQSRT, 6, 1, 1966.

39. Hoshizaki, H. and Lasher, L.E.: Convective and Radiative Heat Transfer to an Ablating Body. AIAA J., 6, 1441, 1968.

40. Evans, J.S. and Schexnayder, C.J., Jr.: An Investigation of the Effect of High Temperature on the Schumann-Runge Ultraviolet Absorption Continuum of Oxygen. NASA Tech. Report R-92, 1961.

41. Chandrasekhar, S. and Elbert, D.D.: On the Continuous Absorption Coefficient of the Negative Hydrogen Ion. V. Astrophys. J., 128, 114, 1958.

42. John, T.L.: Monthly Notice Roy.Astron. Soc., 128, 93, 1964; also 131, 315, 1966.

43. Ohmura, H. and Ohmura, T.: Astrophys. J., 131, 8, 1960; Phys. Rev. 121, 513, 1961.

44. Cooper, J.W. and Martin, J.B.: Phys. Rev., 126, 1482, 1962.

45. Seman, M. and Branscomb, L.M.: Phys. Rev., 125, 1602, 1962.

46. Norman. G.E.: The Role of the Negative Nitrogen Ion N^- in the Production of the Continuous Spectrum of Nitrogen and Air Plasmas. Opt. Spectry., 17, 94, 1964.

47. Boldt, G.: The Recombination of "Minus" Continua of Nitrogen Atoms. Z. Physik 143, 330, 1959.

48. Morris, J.E., Bach, G.R., Krey, R.U., Liebermann, R.W. and Yos, J.M.: Continuum Radiated Power for High-Temperature Air and Its Components, AIAA J., 4, 1223, 1966.

49. Meyerott, R.E., Sokoloff, J., and Nicholls, R.A.: Absorption Coefficients of Air. Report No. LMSC-288052, Lockheed Missiles & Space Co., Sunnyvale, California, September 1959. Also, Geophysics Res. Dir., GRO TR-60-277.

50. Wiese, W.L., Smith, M.W., and Glennon, B.M.: Atomic Transition Probabilities. National Bureau of Standards Report NSRDS-4, 1966.

51. Nicolet, W.E.: User's Manual for the Generalized Radiation Transfer Code (RAD/EQUIL). Report No. UM-69-9, Aerotherm Corporation, Mountain View, California, October, 1969

52. Hilsenrath, J. and Klein, M.: Tables of Thermodynamic Properties of Air in Chemical Equilibrium Including Second Viral Corrections from 1500°K to 15,000°K. Report No. AEDC-TR-65-58, Arnold Engineering Development Center, Tennessee, March 1965.

53. Armstrong, B. and Scheibe, M.: Equilibrium Occupation Numbers and Species Concentrations for Air, Nitrogen, and Oxygen to 24,000°K. Report 6-74-64-33, Lockheed Missiles and Space Company, Sunnyvale, California, June 1964.

54. Lewis, C. H. and Burgess, E.G.: Charts of Normal Shock Wave Properties in Imperfect Air. Report No. AEDC-TDR-64-43, Arnold Engineering Development Center, Tennessee, March 1964.

55. Heron, K.: Shock Tube Gas Dynamic Charts. Part II: Martian Atmospheres (Models G, H, I, J & K). Report TM 65-23, Avco Corporation, Wilmington, Massachusetts, May 1965.

56. Morris, J.S., Krey, R.V. and Garrison, R.L.: Radiation Studies of Arc Heated Nitrogen, Oxygen, and Argon Plasmas. Report No. ARL 68-0103, Avco Cirporation, Wilmington, Massachusetts, May 1968.

57. Allen, R.A.: Air Radiation Tables: Spectral Distribution Functions for Molecular Band Systems. Research Report 236, AVCO-Everett Research Laboratory, Everett, Massachusetts, April 1966.

58. Sherman, M.P. and Kulander, J.L.: Free-Bound Radiation from Nitrogen, Oxygen and Air. General Electric Co. Report R65SD15, May 1965.

59. Kelly, P.S.: Transition Probabilities in Nitrogen and Oxygen from Hartree-Fork-Slater Wave Functions. JQSRT, 4, 117, 1964.

60. Nerem, R.M.: Stagnation Point Heat Transfer in High Enthalpy Flows. Ohio State Univ. Report FDL-TDR-64-41, Part II, March 1964.

61. Gruszczynski, J.S. and Warren, W.R.: Study of Equilibrium Air Total Radiation. AIAA Paper No. 66-103, January 1966. Also Report No. NASA-CR-97931, General Electric Co., King of Prussia, Pa., September 1968.

62. Wood, A.D., Hoshizaki, H., Andrews, J.C., and Wilson, K.H.: Measurements of the Total Radiant Intensity of Air. AIAA Paper No. 67-311, April 1967.

63. Golobic, R.A., and Nerem, R.M.: Shock-Tube Measurements of End-Wall Radiative Heat Transfer in Air. AIAA J., 6, 1741, 1968.

APPENDIX A

THE RADIATIVE PROPERTIES OF SELECTED MOLECULAR BAND SYSTEMS

The contributions of the C_2 and H_2 molecular band systems are from curve fits to radiative data generated with the Patch, Shackleford and Penner "smeared line model" (Ref. A.1), employing the f-number and Franck-Condon factors given in Table A-1.

TABLE A-1

BASIC DATA FOR C_2 AND H_2 BAND SYSTEMS

Species	Band System	f-number and Source	Franck-Condon Factor Source
C_2	Freymark	0.02 from Ref. A.2	Ref. A.4
	Fox-Herzberg	0.05 from Ref. A.2	Ref. A.5
	Mulliken	0.1 from Ref. A.2	Ref. A.4
H_2	Lyman	0.2 from Ref. A.3	Ref. A.6
	Werner	0.4 from Ref. A.3	Ref. A.6

REFERENCES FOR APPENDIX A

A.1 Patch, R. W., Schackleford, W. L., and Penner, S. S.: Approximate Spectral Absorption Coefficient Calculations for Electronic Band Systems Belonging to Diatomic Molecules. JQSRT, 2, 263, 1962.

A.2 Hoshizaki, H. and Lasher, L. E.: Convective and Radiative Heat Transfer to an Ablating Body. AIAA J., 6, 1441, 1968.

A.3 Soshnikov, V. N.: Absolute Intensities of Electronic Transitions in Diatomic Molecules. Soviet Phys., Uspekhi, 4, 425, 1961.

A.4 Nicholls, R. W.: Franck-Condon Factors to High Quantum Numbers Vl: C_2 Band Systems. J. Res. NBS, 69A, 397, 1965.

A.5 Jain, D. C.: Transition Probability Parameters of the Swan and Fox-Herzberg Band Systems of the C_2 Molecule. JQSRT, 4, 427, 1964.

A.6 Patch, R. W.: Vibrational Overlap Integrals for Ultraviolet Bands of H_2. J. Chem. Phys., 41, 1881, 1964.

NASA-Langley, 1970 —— 33 CR-1656